EFFECT OF B-SITE EUROPIUM DOPING ON THE HYDROGEN TRANSPORT PROPERTIES OF BARIUM CERATE

By

JAMES MICHAEL RHODES

A DISSERTATION PRESENTED TO THE GRADUATE SCHOOL
OF THE UNIVERSITY OF FLORIDA IN PARTIAL FULFILLMENT
OF THE REQUIREMENTS FOR THE DEGREE OF
DOCTOR OF PHILOSOPHY

UNIVERSITY OF FLORIDA

2005

To my wife, my son, and my parents.

ACKNOWLEDGMENTS

I thank my family for their love and support. My parents provided me with more than any son deserves. I thank my sisters, Anne and Lynne, for being there for me. I thank Dr. Eric Wachsman for his advice and his support during my time in his group. I would also like to acknowledge the International Consortia for the Conversion of Natural Gas (CANMET) and the National Aeronautics and Space Administration (NASA) for funding my research. I would like to let Dr. Brennan know how much I appreciate his worldly counsel. I also thank the other members of my committee (Drs. Holloway, Sigmund, and Anderson) for sacrificing their time for my education.

I would like to thank all of the friends I have met during my time in Florida. I would particularly like to thank Jay and Rich for all the good times in Oxford Manor and the Reserve. I have to thank Jim "Hacksaw" Stevens and all of the Cabbages for putting up with my antics and for providing me with many great memories. I have to let the Beatty gang know how enjoyable the Rhines' years were because of them. I want Jeanne and Jeremy to know how much I appreciate and value their friendships. I thank Mike, Nabil, Josh, and all the other good people in the MAE building for creating a fun place to work. I must thank Terry for all his hard work in the lab. I would also like to thank Missy Norman for being there to help whenever I need it. I would like to let Keith Duncan know how much I appreciate his time and his advice. I want to thank Jennifer Wrighton for all of her hard work and her support.

Two people provided me with invaluable friendships during the preparation of my dissertation, Abhishek Jaiswal and Brent Gila. I would like to thank Abhishek for all of his help and for all of the good chats. Brent is the most selfless person I know, and has helped me whenever I called. He taught me the true meaning of friendship and of Gator football.

I would be remiss if I did not thank Ara Manukian and Rudy Strohschein (of Analytical Research Systems) for being there when I needed my mistakes repaired.

Lastly and most importantly, I thank the love of my life, Kristi, for her patience, her support, and her love. She had faith in me when I did not have faith in myself. Kristi and Oliver, our newborn son, are the reasons to thank God for each day.

TABLE OF CONTENTS

page

ACKNOWLEDGMENTS iii

LIST OF TABLES viii

LIST OF FIGURES ix

CHAPTER

1 INTRODUCTION 1

2 LITERATURE REVIEW 4

- 2.1 Hydrogen Production Technology 4
- 2.2 Membrane Concepts 5
  - 2.1.1 Palladium Membranes 5
  - 2.2.2 Inorganic Porous Membranes 6
  - 2.2.3 Hydrogen Electrochemical Pump 7
  - 2.2.4 Dual-phase Membranes 7
  - 2.2.5 Dense Ceramic Membranes 8
- 2.3 Proton Conduction 8
  - 2.3.1 Perovskite Oxides 8
  - 2.3.2 Proton Incorporation 9
  - 2.3.3 Proton Conduction Mechanism 10
- 2.4 Structure of Barium Cerate 12
- 2.5 Hydrogen Permeation Membranes 13

3 EXPERIMENTAL APPROACH 25

- 3.1 Sample Preparation 25
- 3.2 Analytical Techniques 26
  - 3.2.1 Scanning Electron Microscopy (SEM) and Energy Dispersive X-ray Spectroscopy (EDS or EDX) 26
  - 3.2.2 X-ray Diffraction (XRD) 26
  - 3.2.3 Electrochemical Impedance Spectroscopy (EIS) 27
  - 3.2.4 Mass Spectrometry (MS) 29
- 3.3 Constructed Equipment 29
  - 3.3.1 Conductivity Apparatus 29
  - 3.3.2 Oxygen Sensor 30

3.3.3 Vacuum System for Mass Spectrometer 31
3.3.4 Permeation Apparatus 32
3.4 Experimental Procedure....33
3.4.1 Conductivity Experiments....33
3.4.2 Permeation Experiments....34

4 ELECTRICAL CONDUCTIVITY INVESTIGATION OF EUROPIUM-DOPED BARIUM CERATE....48

4.1 Introduction....48
4.2 Experimental Methods....49
4.3 Results....50
4.4 Conclusions....53

5 ELECTRONIC CONDUCTION OF EUROPIUM-DOPED BARIUM CERATE....63

5.1 Introduction....63
5.1.1 Measurement Techniques....63
5.1.2 Po_2-dependence of Conductivity....63
5.1.3 Effect of Hydrogen Atmosphere 65
5.2 Experimental Methods....65
5.3 Results....66
5.4 Conclusions....67

6 GLASS SEAL DEVELOPMENT 71

6.1 Introduction....71
6.1.1 Types of High Temperature Seals 71
6.1.2 Membrane-to-Support Sealing Configurations 72
6.1.3 Glass Seal Properties 73
6.2 Experimental Methods....74
6.3 Results....75
6.3.1 Phase One Results 75
6.3.2 Phase Two Results....76
6.3.3 Phase Three Results....77
6.4 Conclusions....79

7 HYDROGEN PERMEATION OF EUROPIUM-DOPED BARIUM CERATE....85

7.1 Introduction....85
7.1.1 Hydrogen Permeation....86
7.1.2 Bulk Diffusion....87
7.1.3 Mixed Controlled Permeation 88
7.1.4 Surface Modification....90
7.1.5 A:B Site Stoichiometry....91
7.2 Experimental Methods....91
7.3 Results....93

7.3.1 Temperature Dependence 93
7.3.2 Hydrogen Partial Pressure Dependence 93
7.3.3 Thickness Dependence 94
7.3.4 Membrane Surface Modification..94
7.3.5 Effect of A:B Stoichiometry...95
7.3.6 Effect of Sm and Yb Dopants...96
7.4 Conclusions...97

8 CONCLUSIONS 108

APPENDIX

A Representative Impedance plots 111

LIST OF REFERENCES..114

BIOGRAPHICAL SKETCH 123

LIST OF TABLES

Table page

2-1. Crystal structure changes of undoped $BaCeO_3$ 12

2-2. Hydrogen permeation fluxes determined by different researchers 17

4-1. Estimated grain sizes (in microns) for all Eu dopant levels and all three sintering temperatures 51

4-2. Bulk densities of $BaCe_{1-x}Eu_xO_{3-\delta}$ bulk samples sintered at 1650°C 52

4-3. Activation energies for conductivity of different Eu dopant levels tested in different atmospheres 53

6-1. Sealing glass names, suppliers, and main components which were studied during phase one and phase two 74

6-2. Composition of ANL Mat43 (mol%) 77

6-3. Glass seal development summary 80

7-1. Activation energies (in eV) for hydrogen permeation flux of membranes of different thickness and different feed-side hydrogen partial pressures 93

7-2. Ambipolar conductivity (in S/cm) estimated from figure 7-4 94

LIST OF FIGURES

Figure page

2-1 Various membrane concepts for hydrogen separation 18

2-2 Cost of palladium from 1992 to 2004........19

2-3 Hydrogen permeabilities of (a) various palladium-based alloys and (b) various pure metals 20

2-4 Conductivities of typical proton conducting perovskite-type oxide ceramics under hydrogen gas atmosphere........21

2-5 Illustrations of two possible proton conduction mechanisms in perovskite oxides ..22

2-6 Predominant proton transfer between oxygen sites (shown by the arrows) in the CeO_6 octahedra of orthorhombically distorted $BaCeO_3$ and $SrCeO_3$. 23

2-7 Crystal structures of $BaCeO_3$ at various temperatures and arrows describing phase transition temperatures 24

3-1 X-ray diffraction by a crystal 37

3-2 (a) Typical current response used to calculate complex impedance and (b) Relationship between capacitive and conductive components of impedance........38

3-3 Equivalent circuit (a) of an ideal Nyqvist plot with semicircles (b) representing mass transport through the grain interiors (III), mass transports across grain boundaries (II), and mass transport at the electrode/electrolyte interface 39

3-4 Ametek quadrupole mass spectrometer head 40

3-5 Schematic of mass filtering with a quadrupole mass spectrometer........41

3-6 Sample holder for conductivity measurements 42

3-7 Oxygen sensor developed for conductivity measurements 43

3-8 Photograph and schematic of gas inlet pumping station 44

3-9 Initial stainless steel permeation apparatus 45

3-10 Schematic of the quartz/alumina apparatus developed for permeation experiments46

3-11 Photograph of permeation apparatus which is clamped and loaded into the test furnace 47

4-1 X-ray diffraction pattern for $BaCe_{0.85}Eu_{0.15}O_{3-\delta}$ before calcining, after calcining at 1100°C, and after calcining at 1350°C ($B=BaCO_3$, $C=CeO_2$, $E=Eu_2O_3$, BCO=barium cerate) 55

4-2 X-ray diffraction patterns of single phase $BaCe_{0.85}Gd_{0.85}O_{3-\delta}$ and $BaCe_{0.85}Eu_{0.85}O_{3-\delta}$ after calcining 1350°C....................56

4-3 Conductivity comparison of $BaCe_{0.85}Gd_{0.15}O_{3-\delta}$ and $BaCe_{0.85}Eu_{0.15}O_{3-\delta}$ in (a) wet forming gas (4% hydrogen/96% nitrogen) and (b) wet air 57

4-4 X-ray diffraction patterns of $BaCe_{1-x}Eu_xO_{3-\delta}$ ($x = 0.05, 0.1, 0.15, 0.20, 0.25$) powders after calcining at 1350°C....................58

4-5 SEM micrographs demonstrating the effect of dopant level and temperature (the marker in the upper left of each micrograph is 10 microns)....................59

4-6 Total conductivity for (a) $BaCe_{0.90}Eu_{0.10}O_{3-\delta}$ and (b) $BaCe_{0.85}Eu_{0.15}O_{3-\delta}$ in dry forming gas, oxygen, and wet nitrogen....................60

4-7 Total conductivity for (a) $BaCe_{0.80}Eu_{0.20}O_{3-\delta}$ and (b) $BaCe_{0.75}Eu_{0.25}O_{3-\delta}$ in dry forming gas, oxygen, and wet nitrogen....................61

4-8 Total conductivity as a function of Eu dopant level for $BaCe_{1-x}Eu_xO_{3-\delta}$ in (a) dry air, (b) wet nitrogen, and (c) dry forming gas 62

5-1 Conductivity measured as a function of oxygen partial pressure....................69

5-2 Conductivity measured as a function of hydrogen partial pressure....................70

6-1 Potential membrane-to-tubular support glass sealing configurations: (a) constrained gravitational sealing. (b) gravitational sealing, and (c) compressive sealing....................81

6-2 Energy dispersive x-ray spectra of (a) an untested membrane surface and (b) a membrane surface after sealing with Elan 63 glass with 10 wt% barium cerate.....82

6-3 Energy dispersive x-ray spectrum of membrane sealed with SEM-COM SCC-5 showing Pb surface contamination....................83

6-4 Energy dispersive x-ray spectra of (a) an untested membrane surface and (b) a membrane surface after sealing with ANL Mat43 glass with 25 wt% barium cerate84

7-1 Schematic of a hydrogen membrane under a hydrogen chemical potential gradient assuming linear kinetics. 99

7-2 Thickness dependence on oxygen flux and γ indicating the transition from a bulk limited regime ($L>>L_c$) to a surface exchange limited regime ($L<<L_c$) 100

7-3 Temperature dependence of hydrogen permeation flux of $BaCe_{0.85}Eu_{0.15}O_{3-\delta}$ at different feed-side partial pressures and thicknesses 101

7-4 Feed-side hydrogen partial pressure dependence of hydrogen permeation flux of $BaCe_{0.85}Eu_{0.15}O_{3-\delta}$ at 750°, 800°, and 850°C for membranes of different thicknesses 102

7-5 Hydrogen permeation flux as a function of inverse membrane thickness................103

7-6 og-Log plot of hydrogen permeation flux as a function of thickness........................104

7-7 Temperature dependence of hydrogen permeation flux for Pt surface modified and unmodified $BaCe_{0.85}Eu_{0.15}O_{3-\delta}$ membranes at different feed-side hydrogen partial pressures 105

7-8 Temperature dependence of hydrogen permeation flux at different feed-side hydrogen partial pressures for varying A:B site stoichiometries (0.99, 1.00, and 1.01)..106

7-9 Temperature dependence of hydrogen permeation flux of $BaCe_{0.85}M_{0.15}O_{3-\delta}$ (M = Eu, Sm, Yb)under different feed-side hydrogen partial pressures (0.01, 0.1, 0.5, 1.0 atm)..107

A-1 Representative impedance spectra used to determine the conductivities of europium-doped barium cerates at different dopant levels (10, 20, and 25 mol%) in dry forming gas. (a) Spectra collected at 600°C and (b) Spectra collected at 800°C ..112

A-2 Representative impedance spectra used to determine the conductivities of 15 mol% Eu-doped barium cerate as a function of hydrogen partial pressure (0.01, 0.1, 0.5, 1.0 atm H_2). (a) Spectra collected at 600°C and (b) Spectra collected at 800°C..113

Abstract of Dissertation Presented to the Graduate School
of the University of Florida in Partial Fulfillment of the
Requirements for the Degree of Doctor of Philosophy

EFFECT OF B-SITE EUROPIUM DOPING ON THE HYDROGEN TRANSPORT PROPERTIES OF BARIUM CERATE

By

James Michael Rhodes

May 2005

Chair: Eric D. Wachsman
Major Department: Materials Science and Engineering

Barium cerate doped with europium on the Ce-site (B-site of the ABO_3 perovskite structure) has been investigated as a potential material for hydrogen separation. Barium cerate doped with 15 mol% europium ($BaCe_{0.85}Eu_{0.15}O_{3-\delta}$) demonstrated higher electrical conductivity in a hydrogen-containing gas stream than gadolinium-doped barium cerate ($BaCe_{0.85}Gd_{0.15}O_{3-\delta}$), which was known to have one of the highest conductivities (0.027 S/cm^2 compared to 0.021 S/cm^2 at 800°C). For europium dopant levels between 5 to 25 mol%, the sample doped with 15 mol% demonstrated higher electrical conductivities in dry forming gas (4% H_2/96% N_2), dry air, and wet nitrogen. The activation energies in dry air (~0.60 eV) were indicative of p-type electronic conduction, and the activation energies in hydrogen-containing gases (~0.35-0.45 eV) were indicative of protonic conduction. With $BaCe_{0.85}Eu_{0.15}O_{3-\delta}$, the onset of n-type electronic conductivity necessary for hydrogen separation was shown to occur at ~600°C.

A gas-tight glass seal was developed to study the hydrogen permeation properties of $BaCe_{0.85}Eu_{0.15}O_{3-\delta}$. The glass seal was a composite of a glass containing strontium oxide, boron oxide, silicon oxide, aluminum oxide, and lanthanum oxide mixed with doped barium cerate powder. The seal would form at temperatures >875°C, allowing for testing down to 650°C.

The effect of temperature, feed-side hydrogen partial pressure, and membrane thickness on hydrogen permeation flux of $BaCe_{0.85}Eu_{0.15}O_{3-\delta}$ was investigated. For the range of thicknesses studied (0.75 to 2.00 mm), the performance of $BaCe_{0.85}Eu_{0.15}O_{3-\delta}$ membranes is under mixed control of bulk diffusion and surface kinetics. This mixed control indicates that investigating $BaCe_{0.85}Eu_{0.15}O_{3-\delta}$ membranes thinner than 0.75 mm would result in a limited increase in hydrogen permeation flux unless measures were taken to improve surface kinetics. The need for improved surface kinetics was confirmed when surface modification using porous platinum on a 1.00 mm membrane resulted in an increase in permeation flux.

CHAPTER 1
INTRODUCTION

On December 4, 2004, the world population was over 6.4 billion.[1] Over 85% of energy consumed by today's population comes from fossil fuel resources.[2] According to the United Nations Population Division, [3] the world population will grow to between 7.4 billion and 10.6 billion by 2050, so energy consumption will continue to increase. Since fossil fuel resources are finite, the demand for an alternative energy supply is growing.

One potential alternative energy supply is hydrogen. Potential applications for hydrogen include fuel for the transportation sector, a source of electric power and heat for homes and industry (along with fuel cells), and an energy source for portable devices. Unfortunately, hydrogen does not exist in a pure form, it exists only in bonded structures. Hydrogen must be produced from fossil fuels, biomass, or water (electrolysis). Methods of extracting hydrogen from biomass (pyrolysis or gasification) and from water (nuclear, photovoltaic, wind, hydro, and geothermal) are currently not efficient or cost effective enough to produce large quantities of hydrogen. Until significant progress is made in producing hydrogen from biomass and electrolysis, the increasing demand for hydrogen must be met by extracting hydrogen from fossil fuel resources. Although this method will initially strain the fossil fuel supply, it will also provide a pathway to a new energy carrier.

Most hydrogen produced in the United States (and about half the world's hydrogen supply) is produced from steam reforming of natural gas or other light hydrocarbons.[4] The three main steps involved in the steam reforming process are steam reforming, water gas shift, and hydrogen purification. The hydrocarbons are initially reacted at high temperatures with steam to produce hydrogen, carbon monoxide, and carbon dioxide. The water gas shift reaction produces more hydrogen and carbon dioxide after converting the carbon monoxide with steam. The mixture of hydrogen and carbon dioxide is separated by pressure swing adsorption (PSA), producing relatively pure hydrogen. In the U.S., most of the hydrogen produced is used in the petrochemical industry and in the manufacturing of ammonia. Steam reforming is only cost effective for large-scale hydrogen production. Therefore, alternative methods must be used to produce hydrogen for the new technologies.

Two alternative methods include partial oxidation of natural gas using an advanced ion transport membrane (ITM) and partial oxidation of coal. Partial oxidation of natural gas requires a source of pure oxygen that reacts with methane (the main constituent of natural gas) to form carbon monoxide and hydrogen. Typically, this method is not cost effective, since a separate process is used to produce the pure oxygen from air. An ITM combines the air separation and the natural gas partial oxidation steps resulting in significant savings.[5] A dense ceramic membrane that conducts both electrons and oxygen ions is used to separate oxygen from air at high temperatures.[5] The oxygen then reacts with a pre-reformed hot mixture of steam and natural gas, forming synthesis gas (syngas), carbon monoxide, and hydrogen. The syngas then passes through a water gas shift reactor producing more hydrogen and carbon dioxide. Currently, the hydrogen is extracted using PSA, which also generates a carbon dioxide gas stream that can be captured and sequestered. Partial oxidation of coal (gasification) produces synthesis gas by combining coal, oxygen, and steam. After further treatment in a water gas shift reactor, the hydrogen is extracted using PSA. The U.S. Department of Energy is investigating the application of gasification to produce electric power and hydrogen in the FutureGen Initiative.

Hydrogen separation membranes could provide a cost effective method to extract high-purity hydrogen from the synthesis gas stream. The need for high hydrogen selectivity limits the potential membrane materials to dense palladium/palladium alloy and dense mixed protonic-electronic conducting ceramics. Palladium membranes have been used to provide high-purity hydrogen for the electronics industry; but they tend to be expensive and to suffer from hydrogen embrittlement. Potential dense ceramic hydrogen membrane materials are perovskite oxides whose proton-conducting properties have been investigated since the early 1980s. Limited fundamental research has been performed on these materials to understand the potential for their application in hydrogen separation.

CHAPTER 2
LITERATURE REVIEW

2.1 Hydrogen Production Technology

As stated in a 1998 Department of Energy report (page 1), [6] "In the next twenty years, concerns about global climate change and energy security will create the platform for the penetration of hydrogen into several niche markets." According to the same report, one-third of the amount of carbon-based emissions in the U.S. is from generating of electricity, while another one-third is from the transportation sector. Hydrogen production technologies will play a major role in reducing these emissions. One possibility would be to use gas separation membranes to produce hydrogen from natural gas, coal, and purge gases which would improve carbon-based emissions by allowing for sequestration of carbon dioxide. At the same time, using hydrogen to power vehicles will also drastically decrease greenhouse gas emissions.

Many hydrocarbon gas streams such as natural gas undergo steam reformation or partial oxidation to produce synthesis gas (syngas) -- a mixture of hydrogen, carbon monoxide, water, and carbon dioxide depending on the process. Hydrogen can be extracted from syngas by cryogenic separation, pressure swing adsorption (PSA), and membrane gas separation.[7] The efficiency of all three techniques depends on the composition of the gas stream. Cryogenic separation is based on relative variation in volatility of gases at low temperatures, and is limited to large-scale operation due (because of its cost). Pressure swing adsorption is a more economical method of hydrogen separation, and is based on selective adsorption of gas stream components.

Commercial gas separation membranes are typically polymer-based, and depend on diffusivity and solubility differences among components for separation. The main disadvantages of all three techniques are the inability to produce a high-purity hydrogen gas stream (>99.9%) and the inability to operate at high temperatures.

Inorganic gas separation membranes appear the most promising for producing high purity hydrogen. The ideal membranes will show high selectivity for hydrogen and will show high hydrogen permeability. For use in the industrial sector, these separation membranes should also be able to withstand high temperatures.

2.2 Membrane Concepts

Permeation membranes can be categorized in various ways; dense or porous, organic or inorganic, and single component or composite. The porous membranes can have a structure that is uniform or asymmetric. Because of the high temperature nature of applications considered in our study, polymeric membranes are not discussed. For hydrogen membranes, a wide array of concepts is possible (Figure 2-1). For ease of explanation, the two sides of the membranes are differentiated as the feed-side (higher hydrogen partial pressure) and the sweep side.

2.1.1 Palladium Membranes

The most investigated type of dense membranes (Figure 2-1a) is palladium-based. Palladium membranes show excellent hydrogen transport properties and hydrogen selectivity, and also show resistance to oxidation at high temperatures.[8, 9] The main problems with Pd membranes are high cost (Figure 2-2), susceptibility to surface poisoning from hydrogen sulfide and carbon monoxide (fouling), and hydrogen embrittlement.[10, 11] Three possible ways to overcome some of these disadvantages include making thinner membranes, using Pd alloys, and using a different metal with high hydrogen permeability. The main issue with using Pd-based membranes for large-scale hydrogen recovery is the high cost (which can be countered partly by making thinner membranes). A variety of metals have been alloyed with Pd such as silver, copper, ruthenium, indium, iron, yttrium, rhodium, and nickel.[12] The effect of some of these alloying elements on the hydrogen permeability of Pd-based membranes is shown in Figure 2-3a. Some of these alloying elements aid in suppressing hydrogen embrittlement.[12] Some other metals such as vanadium, tantalum, and niobium have higher hydrogen permeability than palladium (Figure 2-3b). The main problem with these individual metal membranes was that an oxide layer would form, even under high vacuum conditions.[12] To avoid this problem, some groups have investigated the effect of a Pd coating on the hydrogen permeability of these other metal membranes.[8]

Another benefit of decreasing the thickness of Pd-based membranes is that the hydrogen permeability of these membranes is controlled by bulk diffusion, so it is inversely proportional to membrane thickness.[12] The significant issue with thinner Pd-based membranes is the loss of mechanical integrity. This issue is surmounted by using a porous support to improve the mechanical strength of the thin metal layer. Potential support materials include porous glass (Vycor), alumina, and stainless steel.[9-12] Most current research on Pd-based membranes involves metal layer/porous support composites.

2.2.2 Inorganic Porous Membranes

Another intensely investigated type of membrane is the inorganic porous membrane. Porous membranes are characterized by the type of structure (uniform or asymmetric), and by the width of the pores [defined by the IUPAC as macroporous (>50 nm), mesoporous (between 50 and 2 nm), or microporous <2 nm].[13] Figure 2-1b shows the more commercially used asymmetric structure. The main issue with porous membranes is that even though they exhibit high permeability, they tend to have low hydrogen permselectivity compared to dense membranes. Some materials tested for use as porous hydrogen separation membranes include MFI-type zeolites (ZSM-5 and Silicalite-1),[14] silica,[15] and alumina.[16] Of these materials, zeolites seem the most promising, since they have a regular structure with pores of molecular size, are thermally stable up to ~700°C, and have inherent catalytic activity.[17] Attempts to improve the permselectivity of other porous membranes include impregnating/dispersing them with metals having high hydrogen selectivity such as Pd, Pt, Rh and Ir.[18-20]

2.2.3 Hydrogen Electrochemical Pump

Figure 2-1c illustrates the concept of a hydrogen electrochemical pump. The hydrogen pump takes advantage of a proton-conducting solid electrolyte, sandwiched between two gas-permeable electrically conductive electrodes. Direct current applied to this structure allows for separation, removal, or supply of hydrogen.[21] Iwahara et al. [21-23] have studied a variety of proton conductors, and discussed their possible applications as steam electrolyzers, steam pumps, and membrane reactors for hydrogenation or dehydrogenation.

2.2.4 Dual-phase Membranes

A fourth membrane concept, the dual-phase membrane (Figure 2-1d), takes advantage of the ionic conductivity of one phase (ceramic) and the electronic conductivity of a second phase (metal). The second phase results in an internal short circuit that eliminates the need for external circuitry and electrically conductive electrodes. The metallic phase could also enhance mechanical stability and improve surface reactions. In the case of oxygen permeation membranes, materials with high oxygen ion conductivity (i.e., doped bismuth oxide or stabilized zirconia) are combined with a metal that is known to have good catalytic properties (i.e., silver).[24, 25]

2.2.5 Dense Ceramic Membranes

The final membrane concept is based on mixed ionic-electronic conducting ceramic oxides (Figure 2-1e). Research on this concept requires a proton conducting oxide that also shows sufficient electronic conductivity. The ambipolar conductivity of this oxide allows for the transport of hydrogen across a membrane subjugated to a hydrogen electrochemical potential gradient. Potential oxides are discussed in the next section.

2.3 Proton Conduction

Over the last 25 years, many have studied the high temperature proton-conducting properties of ABO_3 perovskite oxides.[26-32] With the perovskite oxide, the A-site cation is in 12-fold coordination with the oxygen, and the B-site cation is in 6-fold coordination with oxygen. Most of these oxides have an $A^{2+}B^{4+}O_3$ structure where A=Ca, Sr, Ba and B=Zr, Ce. By partially substituting B-site cations with trivalent cations, intrinsic oxygen vacancies are formed. These oxygen vacancies are necessary for proton formation.[27] Potential applications for these oxides include fuel cells, steam electrolyzers, hydrogen gas sensors, and hydrogen pumps.[33] Research on oxides for these applications has focused on achieving high proton conductivity without electronic conductivity. The focus of research must shift toward increasing the electronic conductivity of these oxides, to use them for hydrogen separation membranes.

2.3.1 Perovskite Oxides

The most widely studied of the $A^{2+}B^{4+}O_3$ oxides are strontium cerate ($SrCeO_3$) and barium cerate ($BaCeO_3$), whose proton-conducting properties were first reported by Iwahara et al.[26, 27] This intense investigation is because these oxides show the highest proton conductivity (Figure 2-4). A variety of dopant cations have been investigated with these cerates. Iwahara et al. [26] studied the proton conductivity of $SrCeO_3$ doped with Yb, Y, Sr, Mg, Zn, In , Nd, Sm, and Dy. After their study, most of the research on SrCeO3 focused on doping with 5 mol% Yb.[28, 34-37] Research on $BaCeO_3$ never focused on one particular dopant or dopant level. Some of the dopant cations include Y, Nd, La, Ca, Sm, Gd, Yb, and Dy (which were doped at levels from 5 to 20 mol%).[27, 31, 32, 38]

2.3.2 Proton Incorporation

Protons are not an inherent part of the oxide structure. The introduction of protons into a perovskite oxide lattice generally occurs by interaction with a moisture-containing atmosphere or hydrogen atmosphere. Reaction of these gas streams with the oxide can be written using Kröger-Vink notation. With this notation, Vo·· represents oxygen vacancies, Oox represents oxide ions on an oxygen lattice site, Hi· represents interstitial protons, OHo· represents protons associated with oxide ions on an oxygen lattice site, and e' represents electrons. For these reactions, OHo· is preferable to Hi· (interstitial protons), since protons are not free in the perovskite lattice but are bound to oxide ions.[39] In a moisture-containing atmosphere, the dissolution of water vapor into the oxide lattice [40] can be expressed by Equation 2-1,

$$H_2O(gas) + V_o^{\cdot\cdot} + O_o^x \leftrightarrow 2\,OH_o^{\cdot} \qquad (2\text{-}1)$$

Alternatively, in a hydrogen atmosphere, protons can be incorporated directly into the oxide lattice along with electrons.[41]

$$\tfrac{1}{2}\,H_2\,(gas) + O_o^x \leftrightarrow OH_o^{\cdot} + e' \qquad (2\text{-}2)$$

Fundamental studies of oxide proton conductors have focused on the interaction of water vapor with oxides, rather than the direct reaction with hydrogen.[40, 41] The interaction of water vapor is treated as two processes: the absorption of an hydroxide ion by oxygen vacancies and the protonation of a lattice oxide ion.[42] The overall result of this interaction is two equivalent protons in the oxide lattice. Experimental and simulation research describing the transport of protons through perovskite oxide lattices supports using the same treatment for protons incorporated directly from a hydrogen atmosphere as is used for protons incorporated from water vapor.

2.3.3 Proton Conduction Mechanism

Two models were proposed to describe proton transport in oxides: the "vehicle mechanism" and the Grötthuss or "free migration" mechanism.[41, 43] Simple cartoons illustrate these mechanisms (Figure 2-5).[43] With the vehicle mechanism, the proton moves as a passenger on a vehicle molecule or ion (e.g., H_3O^+). Diffusion of this vehicle, coupled with diffusion of an unprotonated molecule in the opposite direction, results in net transport of protons. With the Grötthuss mechanism, the proton attaches to a stationary ion (e.g., O_o^x), undergoes a reorientation step, and then transfers to another stationary ion.

Over the last decade, general agreement has been that in ABO_3 perovskites, protons transfer between fixed oxygen sites via the Grötthuss mechanism, at high temperatures. This agreement is a result of research on perovskite oxides, using isotope effect measurements (H^+/D^+).[44-47] Molecular dynamic studies of $BaCeO_3$, $BaZrO_3$, $BaTiO_3$, and $CaZrO_3$ contributed additional support for the Grötthuss mechanism as the method of proton diffusion in both cubic and orthorhombic perovskites.[48-50] Munch et al. [48, 49] determined that the reorientation process occurs relatively fast (10^{-12} s) compared to the proton transfer process (10^{-9} s). This would indicate that the proton transfer process is the rate-limiting step. Contradictory research shows strong red-shifted OH-stretching absorptions in the infrared spectra, indicative of strong hydrogen bond interactions that favor fast proton transfer reactions rather than fast reorientation processes.[51]

The extensive work of Kreuer and his colleagues has been pivotal to the fundamental understanding of proton conduction in ABO_3 perovskites.[42, 46, 51-53] Three important parameters discussed in their work are the structural oxygen separation (Q_o), the oxygen separation coordinate (Q), and the stiffness of the B-O bond. Cubic perovskites with large lattice constants that correspond to large structural oxygen separation show the highest proton diffusivities.[51] This high proton mobility can be explained by increased thermal vibrations of oxygen. Dynamics of these oxygen vibrations are influenced by the "softness" of the oxygen separation coordinate, and by the stiffness of the B-O bond. Materials with high thermal expansion coefficients may exhibit this softness, which is necessary for rapid proton transfer.[46] The stiffness of the B-O bond is a result of the covalency of the B-O bond. Low covalency in a loosely packed oxide structure with a large Q_o, (such as $BaCeO_3$), allows for extended oxygen vibrations and an energetically low proton transition, which facilitates proton transfer.[51]

The previous discussion is limited to cubic perovskites where neighboring oxygens are treated as equivalent sites. Perovskites that have a reduced symmetry (such as $SrCeO_3$) must be treated differently. The orthorhombic distortion of $SrCeO_3$ doped with yttria has a major effect on the arrangement of the lattice oxygen.[52] The cubic oxygen sites degenerate to two sites (O1 and O2) with occupancy probabilities of 1/3 and 2/3 respectively. These oxygen sites have different chemical interactions with the cations, and exhibit different binding energies for protons, due to different electron densities (basicities). $BaCeO_3$ also exhibits some structural distortion (discussed in the next section). In $SrCeO_3$, the most basic oxygen site is O1; while in $BaCeO_3$, O2 is most basic.[42] Proton transfer between oxygen sites in both $SrCeO_3$ and $BaCeO_3$ is shown in figure 2-6. The long-range transport between O2 sites in $BaCeO_3$ should be easier than transport between O1 and O2 sites in $SrCeO_3$. This difference in proton transport is a possible reason for lower conductivity in $SrCeO_3$.

2.4 Structure of Barium Cerate

The crystal structure of $BaCeO_3$ has been investigated by x-ray and neutron diffraction and has been classified as cubic, tetragonal, and orthorhombic depending on the researcher.[54-59] Potential reasons for the different structural characterization include variations in material preparation, improvements in refinement methods, or technological advances in analytical equipment. Intense study of $BaCeO_3$ indicates that the room temperature structure is orthorhombic. Although structural characterization at room temperature is important, it is not as vital as knowledge about structure at the higher temperatures, where proton conduction is typically investigated. Neutron diffraction studies by Knight indicate that undoped $BaCeO_3$ undergoes three structural changes between 373K and 1173K (Table 2-1 and Figure 2-7).[58]

Table 2-1. Crystal structure changes of undoped $BaCeO_3$

Crystal structure change	Space group change	Type of transition	Temperature (K)
Orthorhombic to orthorhombic	Pmcn to Incn	Continuous	563
Orthorhombic to rhombohedral	Incn to F32/n	Discontinuous	673
Rhombohedral to cubic	F32/n to Pm3m	Continuous	1173

Knight initially suggested from preliminary results that doping with 10 mol% Y shifted the orthorhombic to rhombohedral transition approximately 100K higher.[58] In a later work, Knight stated that for both Y- and Nd- doping, the phase transition sequences stayed the same but the width of the phase fields changed.[60] Compared to the undoped $BaCeO_3$, the width of the Incn orthorhombic phase increased, while the width of the F32/n rhombohedral phase decreased. These structural changes have the most influence on the oxygen sites available for proton transfer. The orthorhombic to orthorhombic transition has little effect on the types of oxygen sites; and proton transfer still is most likely to occur between O2 sites. Transition to the rhombohedral phase results in a single type of oxygen site, and a more open structure (which, according to discussion of cubic $BaCeO_3$ in the previous section, should lead to improved proton transfer).

2.5 Hydrogen Permeation Membranes

The proton conductivity of various perovskite-type oxides has been examined extensively, but few researchers have addressed the hydrogen permeation of these materials.[61-65] These reports of hydrogen permeation have focused on $SrCeO_3$ acceptor doped with Tm, Y, or Yb. Different testing conditions and analytical methods have been used to determine the hydrogen permeation flux.

Hamakawa et al. [61] tested a $SrCe_{0.95}Yb_{0.05}O_{3-d}$ membrane (1 mm thickness) at 900°C using asymmetrical conditions with a 1% H_2/He feed gas and an O_2/Ar (or just Ar) sweep gas. The hydrogen permeation flux was determined using a gas chromatograph to analyze the amount of H_2 in the Ar sweep gas, or using a dew point hygrometer to determine the amount of H_2O evolved in the O_2/Ar sweep gas. Hydrogen was not present in the Ar sweep gas, indicating no flux; while the amount of H_2O evolved increased with increasing oxygen partial pressure in the sweep gas. The maximum water evolution rate of $\sim 2.3 \text{ X } 10^{-6}$ mol/cm^2-min was measured in 100% O_2 sweep gas which equates to a hydrogen flux of $\sim 3.8 \text{ X } 10^{-8}$ mol/cm^2-s. Hydrogen pumping experiments were also performed on samples, so a porous platinum coating was on both sides of the membrane, even under open circuit conditions.

Guan et al. [62] studied a $SrCe_{0.95}Y_{0.05}O_{3-d}$ membrane (1.1 mm thickness) using symmetrical conditions, with 4%H_2/Ar on one side and 0.488% H_2/Ar on the other side. The hydrogen permeation flux was estimated from measured short-circuit currents and was also predicted from measured proton conductivities. At 800°C, the hydrogen flux was estimated from proton conductivity and short-circuit measurements as 0.072 cm^3(STP)/cm^2-min (4.9 x 10^{-8} mol/cm^2-s) and 0.023 cm^3(STP)/cm^2-min (1.6 x 10^{-8} mol/cm^2-s), repectively. There calculations assume that the kinetics of the surface reaction are infinitely fast.

Qi and Lin [63] investigated $SrCe_{0.95}Tm_{0.05}O_{3-d}$ membranes (1-3 mm thicknesses) using asymmetrical conditions with H_2/He feed gas streams and O_2/N_2 sweep gas streams. The hydrogen permeation flux was calculated from the rate of water evolved in the sweep gas stream. This study determined the effect of temperature, membrane thickness, and upstream and downstream hydrogen partial pressures. A hydrogen permeation flux of ~3 X 10^{-8} mol/cm^2-s was obtained at 900°C with a 1.6 mm thick membrane tested with a 10% H_2/He feed gas and an air sweep gas.

Li and Iglesia [64] investigated a $SrCe_{0.95}Yb_{0.05}O_{3-d}$ membrane (1 mm thick) at 677°C using both symmetrical and asymmetrical conditions with a H_2/He feed gas and a N_2 or N_2/O_2 sweep gas. The hydrogen permeation flux was determined by measuring the water concentration in the sweep gas, in both short-circuit and open-circuit conditions. Under symmetrical conditions (H_2 feed and N_2 sweep), the flux was ~1.5 x 10^{-8} mol/cm^2-s for the short-circuit membrane and ~1.0 x 10^{-8} mol/cm^2-s for the open-circuit membrane.

Under asymmetrical conditions (H_2 feed and 10%O_2/N_2 sweep), the flux was ~15 x 10^{-8} mol/cm^2-s for the short-circuit membrane and ~1.5 x 10^{-8} mol/cm^2-s for the open circuit sample. The short circuit resulted from attaching platinum wires to both sides of the membrane, using a silver conductor ink; so the porous silver was also present for the open-circuit measurements.

Hamakawa et al. [65] studied thin film membranes of $SrCe_{0.95}Yb_{0.05}O_{3-d}$ on porous supports at 677°C. The tests were done in symmetrical conditions with a H_2/N_2 feed gas and a He sweep gas. The hydrogen permeation rates were determined using a mass spectrometer, and confirmed by a humidity meter (O_2 was added downstream from the mass spectrometer). Films of three different thicknesses (2, 80, and 140 microns) were analyzed, as well as a 1 mm thick unsupported sample. Hydrogen permeation fluxes of the different samples varied linearly with inverse thickness, which indicates that the flux through the membrane is limited by bulk diffusion. The flux in a sweep gas with a hydrogen partial pressure of 40 kPa was ~83.3 x 10^{-8} mol/cm^2-s for the 2 micron membrane, and ~0.3 x 10^{-8} mol/cm^2-s for the 1 mm membrane. The researchers stated that, although the 2 micron membrane was covered by a thick porous layer, this membrane was unlikely to be affected by surface processes, because of the slow nature of the bulk transport.

In a more recent study, Song et al [66] studied the hydrogen permeation of $SrCe_{0.95}Eu_{0.05}O_{3-d}$ and $SrCe_{0.95}Sm_{0.05}O_{3-d}$ using mass spectrometry. The tests were performed using hydrogen-containing feed-gases and a He sweep gas. The samples were 1.72 mm thick and were tested from 650°C to 850°C. Under 100% H_2 feed-gas at 850°C, the $SrCe_{0.95}Eu_{0.05}O_{3-d}$ and $SrCe_{0.95}Sm_{0.05}O_{3-d}$ had hydrogen permeation fluxes of 3.19 x

10^{-9} mol/cm^2-s and 2.33 x 10^{-9} mol/cm^2-s, respectively. The results of all hydrogen membrane research are summarized in table 2-2.

Although doped barium cerates tend to have the highest protonic conductivities at high temperatures, they have not been thoroughly studied as a potential hydrogen separation membrane material. Limited research focused on improving the electronic conduction in barium cerates, which is necessary for hydrogen permeation, has been performed. Also, the focus of most high temperature hydrogen separation membrane studies has been on doped strontium cerates which have a lower protonic conductivity than barium cerate. Most of these hydrogen separation studies have failed to introduce a fundamental understanding of membrane performance (the role of bulk diffusion and surface exchange kinetics). Our studies will focus on improving the electronic conductivity of doped barium cerate, on developing a seal for this material for membrane analysis, and on understanding the hydrogen separation properties of doped barium cerate.

Table 2-2. Hydrogen permeation fluxes determined by different researchers

Authors	Membrane material and size	Test gases	Temp. (°C)	Analytical technique	Results (10^{-8} mol/cm^2-s)
Hamakawa [61]	$SrCe_{0.95}Yb_{0.05}O_{3-\delta}$ 1 mm	Feed: 1% H_2/He Sweep: 100% O_2	900	H_2O evolution	3.8
Guan [62]	$SrCe_{0.95}Y_{0.05}O_{3-\delta}$ 1.1 mm	Feed: 4% H_2/He Sweep: 0.488% H_2	800	Calculated from proton conductivity and from short-circuit current	4.9 1.6
Qi [63]	$SrCe_{0.95}Tm_{0.05}O_{3-\delta}$ 1-3 mm	Feed: 10% H_2/He Sweep: Air	900	H_2O evolution	3.0 (1.6 mm membrane)
Li [64]	$SrCe_{0.95}Yb_{0.05}O_{3-\delta}$ 1 mm	Feed: 100% H_2 Sweep: 100% N_2	677	H_2O evolution	1.0
Li [64]	$SrCe_{0.95}Yb_{0.05}O_{3-\delta}$ 1 mm	Feed: 100% H_2 Sweep: 10% O_2/N_2	677	H_2O evolution	1.5
Hamakawa [65]	$SrCe_{0.95}Yb_{0.05}O_{3-\delta}$ 2 ,80, 140 μm & 1 mm	Feed: 40% H_2 Sweep: 100% He or N_2	677	Mass Spectrometry and H_2O evolution	83.3 (for 2 μm) 0.3 (for 1 mm)
Song [66]	$SrCe_{0.95}Eu_{0.05}O_{3-\delta}$ 1.72 mm	Feed: 100% H_2 Sweep: 100% He	850	Mass Spectrometry	0.32
Song [66]	$SrCe_{0.95}Sm_{0.05}O_{3-\delta}$ 1.72 mm	Feed: 100% H_2 Sweep: 100% He	850	Mass Spectrometry	0.23

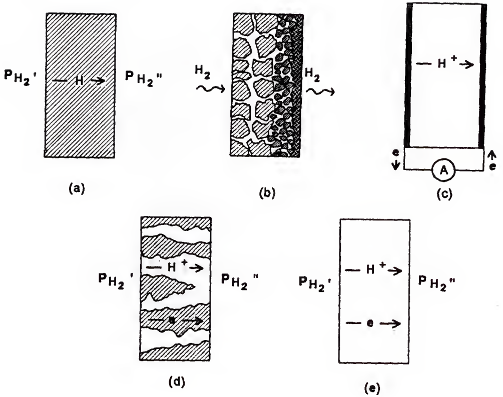

Figure 2-1. Various membrane concepts for hydrogen separation a) dense metallic membrane, b) asymmetric porous membrane consisting of a support, an intermediate layer, and a barrier layer with graded porosity, c) solid electrolyte hydrogen pump, d) dual-phase membrane, and e) dense mixed-conducting oxide membrane [from ref 67]

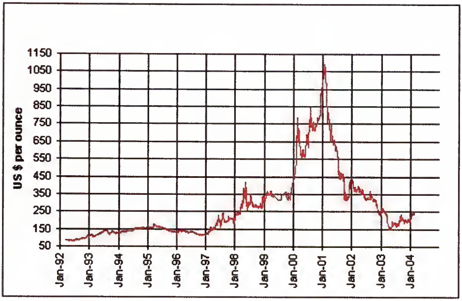

Figure 2-2. Cost of palladium from 1992 to 2004

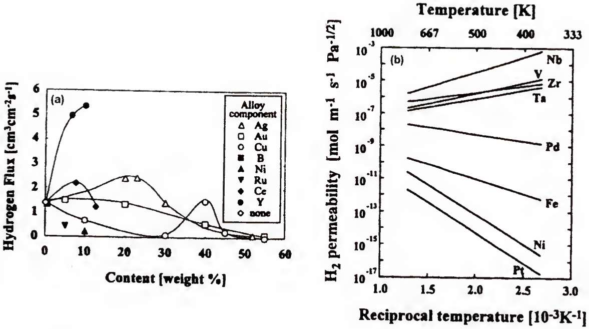

Figure 2-3. Hydrogen permeabilities of (a) various palladium-based alloys and (b) various pure metals [from ref 12]

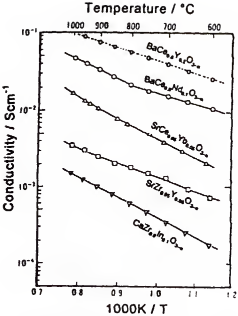

Figure 2-4. Conductivities of typical proton conducting perovskite-type oxide ceramics under hydrogen gas atmosphere [from ref 68]

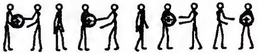

Grotthuss mechanism
(structure diffusion)

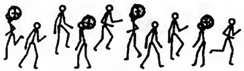

vehicle mechanism

Figure 2-5. Illustrations of two possible proton conduction mechanisms in perovskite oxides [from ref 43]

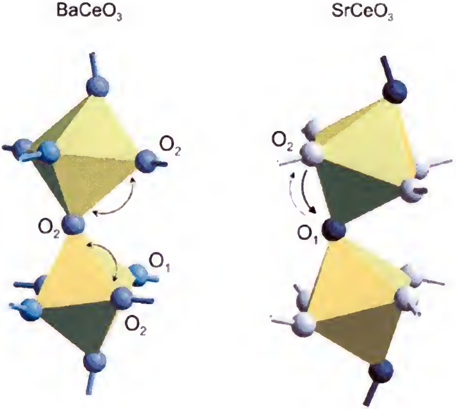

Figure 2-6. Predominant proton transfer between oxygen sites (shown by the arrows) in the CeO_6 octahedra of orthorhombically distorted $BaCeO_3$ and $SrCeO_3$. The degree of basicity is indicated by the darkness of the oxygen sites (darker=more basic) [from ref 69]

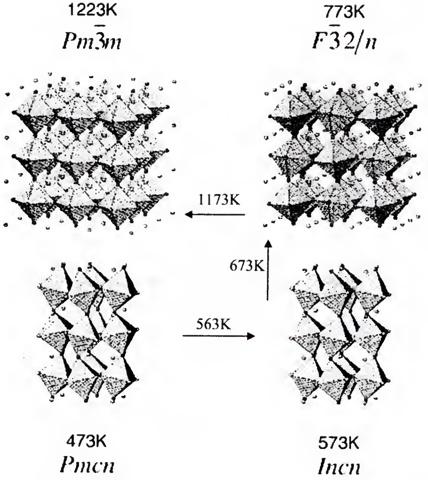

Figure 2-7. Crystal structures of $BaCeO_3$ at various temperatures and arrows describing phase transition temperatures [from ref 60]

CHAPTER 3
EXPERIMENTAL APPROACH

3.1 Sample Preparation

Powders used for all research were prepared using solid state reaction. The constituent powders were barium carbonate (Alfa Aesar 99.95%), cerium (IV) oxide (Alfa Aesar REacton 99.99%), and europium (III) oxide (Alfa Aesar REacton 99.9%). The initial compositions were mixed in a stoichiometric ratio to yield compositions of the form $BaCe_{1-x}Eu_xO_{3-\delta}$ ($x = 0.05, 0.10, 0.15, 0.20$, and 0.25). The powders were ball milled in polyethylene bottles using zirconia media and ethanol for 10 hrs. The resultant powders were dried then calcined in alumina crucibles at 1100°C for 10 hours using a Lindberg Model BF51314C box furnace. The powders were mixed again then calcined in alumina crucibles at 1350°C for 10 hours.

Pellet samples were prepared using steel dies with three different diameters – 0.315 inches (dilatometry), 0.5 inches (impedance), and 1.125 inches (permeation). The powders were uniaxially pressed at ~50 MPa then isostatically repressed at 250 MPa. The uniaxial press is a Carver model C (press no. 3851), and the cold isostatic press is a Fluitron CP2-2-60. The pellets were sintered in the Lindberg box furnace on a bed of powder with the same composition. After sintering, the pellets were polished using SiC paper. Samples for scanning electron microscopy were polished from 600 grit paper to 1 micron polishing paste and nitric acid etched.

3.2 Analytical Techniques

3.2.1 Scanning Electron Microscopy (SEM) and Energy Dispersive X-ray Spectroscopy (EDS or EDX)

The scanning electron microscope used for analysis of particles and of sintered microstructures in this work was a JEOL 6400 SEM. An SEM uses secondary electrons and backscattered electrons produced as a result of electron beam-solid interactions to image the surface of a material. Secondary electrons provide topographical information about the surface, while backscattered electrons provide compositional information.

The electron beam is generated using an electron gun which consists of a tungsten filament, a Wehnelt cylinder (grid cap), and an anode. The electron gun supplies an electron beam with an accelerating voltage of 0.1-30 kV. The beam then travels through condenser lenses and an objective lens which contains deflection (scan) coils, the stigmator, and the beam-limiting aperture.

SEM images are generated by rastering the focused beam using the deflection coils over the surface of the sample. The focused beam interacts with the surface of the sample resulting in the generation of secondary electrons, backscattered electrons, and x-rays. Detection of all three species is possible with different detectors. Secondary and backscattered electron detectors are used to transform signal into images, and an energy dispersive x-ray detector can produce a spectrum of x-ray energies or an x-ray map of the surface.

3.2.2 X-ray Diffraction (XRD)

X-ray diffraction was used to analyze the phase purity of powders and of solids processed during this research. The diffractometer was a Phillips model APD 3720 operated at 40 kV and 20 mA. The wavelengths of the Cu K_α doublet (Ni filtered) used for analysis were 1.54056 Å and 1.54439 Å. The typical diffractometer scan ran from 20° to 80° 2Θ with a step size of 0.01° and a scan speed of 0.02° per second.

Figure 3-1 illustrates x-ray diffraction resulting from the interaction of x-rays with periodically arranged atoms in a crystalline material. Knowing the wavelength of the characteristic x-rays and 2Θ, Bragg's law, equation 3-x, can be applied to obtain the d-spacing between the atomic planes.

$$\lambda = 2d\sin\Theta \qquad (3\text{–}1)$$

With Bragg's law, λ is the wavelength of the incident x-ray, d is the spacing between planes, and Θ is the measured peak position. The d-spacings can be used to calculate the lattice parameters for crystalline materials.

3.2.3 Electrochemical Impedance Spectroscopy (EIS)

Electrochemical impedance spectroscopy (EIS) has become an important technique for analyzing solid state systems. This non-destructive technique utilizes the frequency dependence of individual processes in a sample to separate out their response. These processes occur in the bulk electrolyte, in the grain boundaries, and at the electrode/electrolyte interface.

The impedance in this research was measured using a Solartron 1260 frequency response analyzer (FRA) over a frequency (f) range of 10^7 to 10^{-1} Hz. With the FRA, a small amplitude, sinusoidal voltage is applied, equation 3-2.

$$v(t) = V\sin(\omega t) \qquad \text{where } \omega = 2\pi f \qquad (3\text{-}2)$$

The voltage produces sample polarization resulting in a current response, equation (3-3), with the same frequency but different phase and amplitude shown in figure 3-2a.[70]

$$i(t) = I\sin(\omega t + \Theta) \qquad (3\text{-}3)$$

The ratio of the voltage response to the current response is called the impedance, $Z(\omega)$.

$$Z(\omega) = V \sin(\omega t) / I \sin(\omega t + \Theta) \quad (3\text{-}4)$$

The impedance is a complex quantity which can be represented in Cartesian and polar coordinates shown in figure 3-2b. By analyzing the impedance in this form, the real conductive component (Z') and imaginary capacitive component (Z") parts can be separated and the absolute value of impedance and phase shift can be calculated

$$Z' = a \cos \Theta \text{ and } Z'' = b \sin \Theta \quad (3\text{-}5)$$

$$|Z| = (Z'^2 + Z''^2)^{0.5} \quad (3\text{-}6)$$

$$\Theta = \arctan (b/a) \quad (3\text{-}7)$$

The data is typically represented with a Nyquist or Cole-Cole plot. The Nyquist plot shows the real part of impedance plotted against the imaginary part. The ideal Nyquist plot of a polycrystalline solid electrolyte, shown in figure 3-3, consists of a series of semicircles representing each of the various processes – mass transport through the grain interior (R_L, C_L), across the grain boundaries (R_{gb}, C_{gb}), and across the electrode/electrolyte interface (R_p, C_{dl}). These semicircles can be modeled using a series network of resistors in parallel with capacitors.

In non-ideal systems, the semicircles can be replaced by depressed arcs which may significantly overlap due to the distribution of time constants. To prevent overlapping, the time constants need to be at least two orders of magnitude apart.[71] The equivalent circuits of the non-ideal system will include constant-phase elements (CPE) instead of capacitors.

3.2.4 Mass Spectrometry (MS)

Gas spectra were collected using a Dycor Quadlink QMS100 quadrupole mass spectrometer (MS) from Ametek, Inc. The MS, also referred to as a residual gas analyzer (RGA), separates and measures ions according to mass to electric charge (m/z) ratio. The Ametek MS, shown as a schematic in figure 3-4, consists of an ionization source, a mass filter, and an ion detector. The ionization source uses a filament from which electrons are thermally emitted and collide with gas molecules in the vacuum system. These ions are focused into the quadrupole mass filter composed of four rod-shaped electrodes having parallel alignment as illustrated in figure 3-5.[72] Opposing rods are paired and have equivalent potentials. This potential consists of a DC voltage and a superimposed high-frequency AC voltage supplied by a RF power supply. Two rods have a positive dc potential while the other two have a negative dc potential. The rod pairs work together as high and low pass filters which allows ions of a particular m/z ratio to pass through the quadrupole filter with a stable oscillation. Ions of all other m/z ratios follow unstable paths and eventually are collected by the rods before exiting the mass filter.[73] The ions of the particular m/z ratio which pass through the filter are detected using a Faraday cup detector.

3.3 Constructed Equipment

3.3.1 Conductivity Apparatus

The apparatus for conductivity tests consists of two main parts the sample holder (shown in figure 3-6) and a quartz tube. The sample holder has a Pyrex end cap fused to a quartz sample tube with a quartz push rod for holding the test leads against the sample. The Pyrex end cap has two threaded ports for the gas inlet and outlet, one threaded port for the quartz push rod, and two holes for the alumina tubes which hold the test leads (0.5

mm diameter gold wire). The face of the end cap has a groove for a silicone rubber o-ring which compresses against a quartz flange on the furnace tube using a stainless steel clamp. The end of the quartz sample tube is partially cut out for sample loading. A K-type thermocouple is inserted inside the quartz push rod and is used to control the temperature of the furnace. The gold test leads are soldered to gold-coated pins used in coaxial male fittings. All threaded ports use rubber o-rings for compression seals. All other potential holes were sealed with silicone RTV sealant.

3.3.2 Oxygen Sensor

Some conductivity experiments required monitoring the oxygen partial pressure in the test gas stream. For these experiments, an inexpensive oxygen sensor was developed. A stainless steel casing was designed to fit a four-wire automotive oxygen sensor. The final sensor is shown in figure 3-7. The casing was tapped to fit the threads of the automotive sensor and machined to fit the protective shield and stabilized zirconia sensor. A small hole was drilled through the center of the casing for gas flow to the sensor. A 1/8" Swagelok® fitting was welded to the top of the casing so a 1/8" Swagelok® tee fitting could be attached for gas flow and for the thermocouple. Another 1/8" Swagelok® fitting was welded near the base of the casing for gas exhaust. The two wires for the internal heater were connected to a 14 Vdc plug. The heater resulted in an initial temperature ~150-200°C. For adequate sensor response, the temperature of the sensor had to be increased so heating tape was wrapped around the casing followed by a layer of fiberglass insulation. The heating tape was controlled using a variable transformer (Variac). The thermocouple at the tip of the oxygen sensor was used to monitor the temperature. The temperature was maintained from 600-800°C. The oxygen partial pressure was calculated using the Nernst equation using $Po_2(II) = 0.21$ atm.

$$E = (RT/4F) \ln[Po_2(I)/Po_2(II)] \quad (3\text{-}8)$$

The accuracy of the sensor was confirmed using a series of H_2/H_2O mixtures and comparing the measured oxygen partial pressures to the thermodynamically calculated values. A baseline measurement was acquired using air at the same flow rate as the test gas.

3.3.3 Vacuum System for Mass Spectrometer

The initial mass spectrometer and vacuum system assembly consisted of the following parts:

- BOC Edwards pumping station
- Vacuubrand MD4 diaphragm pump, Edwards EXT250Hi turbomolecular pump, Edwards active thermocouple and ion gauges
- A & N conical flange and 4-way cross (for the mass spec head, the ionization gauge, the gas inlet, and a viewport)
- Ametek Q100MS analyzer with a Dycor Quadlink Power Supply
- Glass Capillary tube and 3-way metering valve

The test gas was introduced to the vacuum chamber using the three-way metering valve and the capillary tube allowing for a pressure drop from atmospheric pressure to $\sim10^{-6}$ torr. Pressures below 10^{-5} torr were required for operation of the Q100MS analyzer head. The main issues with this system were the lack of pressure control in the vacuum chamber due to the capillary, the brittle nature of the capillary, and the high background levels due to the diaphragm pump.

Modifications to the system were made to overcome these difficulties. The capillary was replaced with a separate gas inlet pumping station and the diaphragm pump was replaced with an Edwards E2M5 mechanical pump. The pumping station, represented photographically and schematically in figure 3-8, used the Vacuubrand MD4 diaphragm pump, a Granville Phillips servo driven valve assembly and 216 pressure flow controller, and a metering valve to control the pressure at the gas inlet. The gas is introduced to the mass spectrometer vacuum chamber through a 25 micron orifice and a Thermo Vacuum Generators UHV valve (ZCRT97TU). The pumping station allows complete control of the pressure in the vacuum chamber from 5 X 10^{-6} to 1 X 10^{-7} torr.

3.3.4 Permeation Apparatus

The most important feature of any permeation apparatus is gas-tight separation of the permeate gas side and the feed gas side. The initial apparatus, shown in figure 3-9, consisted of 0.25 inch metal tubing welded to a three-pronged disc and to a mating three-hold disc. The two metals used for different setups were 304 stainless steel and inconel. The stainless steel tended to oxidize at high temperatures requiring extensive cleaning which limited the lifetime of the apparatus. The inconel did not oxidize as much as the stainless steel, but the inconel did contain chromium which would deposit on the surface of membranes. Another limitation of this style of apparatus is the inability to consistently seal the membrane due to mechanical loading. The mechanical loading of the sample would occasionally result in fracture of the membrane or in excess flow of the sealing glass that would cover the surface of the membrane. The difficulties with this apparatus led to the development of a quartz tube/alumina tube apparatus (Figure 3-10) which was used for the main permeation experiments.

The quartz/alumina apparatus consists of four main parts: (1) the quartz reactor tube, (2) the quartz push rod, (3) the 1.0 inch alumina tube, and (4) the Pyrex compression coupler. The main features of the quartz reactor tube are the 0.25 inch quartz tube joined to a ring seal just above the main sample area. This tube focuses the feed gas on the surface of the membrane while eliminating the dead space at the top of the tube. The alumina tube is joined to the quartz reactor tube with a Pyrex compression fitting. The alumina tube and the quartz push rod are connected with the Pyrex coupler (basically two compression fittings and a gas outlet to the mass spectrometer). The push rod contains a 0.25 inch quartz tube for the sweep gas. The push rod is placed as close as possible to the membrane to allow the sweep gas to carry all permeating gas to the mass spectrometer. The diameter of the push rod is similar in size to the inner diameter of the alumina tube minimizing the dead volume thus increasing response time.

The apparatus is loaded into a custom-made furnace and stabilized with a combination of clamps and fittings (Figure 3-11). Ultra-torr fittings are used to connect the gas lines to the gas inlets. The gas outlet to the mass spectrometer uses a Pyrex compression fitting. The temperature of the furnace is controlled with a Eurotherm 2408 controller.

3.4 Experimental Procedure

3.4.1 Conductivity Experiments

The conductivity experiments were performed using the conductivity apparatus and the Solartron 1260 frequency response analyzer (FRA). The sample was connected by contacting each side of the sample with the gold wire leads then using the quartz push rod to apply a compressive force. The test leads were connected to the FRA using two pairs of 1 meter long coaxial cables. The coaxial cables pairs consisted of one cable for signal generation and one cable for measurement. The data was collected using ZPlot® for Windows software developed by Scribner Associates, Inc. Each measurement was performed using a frequency sweep controlling the applied a.c. voltage and measuring the current (Ctrl E: Sweep Freq tab on the software). The amplitude of the applied voltage was between 50-100 mV. The frequency sweep was from 10 MHz to 0.1 Hz. Before any experiments were performed, nulling files were collected which reduce the effect of the test leads and the sample holder from the experimental data. The test data was collected after allowing the sample to equilibrate at each temperature and gas condition. The equilibration times varied from 30 minutes to 3 hours. The equilibration time was determined by comparing results from consecutive measurements typically 15 minutes apart. For samples tested as a function of temperature, the samples were heated to the highest temperature then tested with decreasing temperature.

The data was analyzed using ZView® for Windows software (also created by Scribner Associates, Inc). The data was fit using equivalent circuits. Most samples consisted of a high frequency (bulk), middle frequency (grain boundary), and low frequency (electrode) contributions at temperatures between 200°-500°C. At higher temperatures, only high frequency (bulk) and low frequency (electrode) contributions could be resolved.

From the fitting procedure, the resistive component of the different processes could be estimated. For the data with three components, the bulk and grain boundary resistances could be separated. At high temperature, only one component could typically be resolved which was generally assumed to be from the bulk. With the measured resistances (R), the conductivity (σ) could be calculated using the cross-sectional area of the sample (A) and the sample length (l) using equation 3-9. The conductivity is reported in siemens/centimeter (S/cm) where S is equivalent to 1/ohm ($1/\Omega$).

$$\sigma = l/(RA) \qquad (3\text{-}9)$$

3.4.2 Permeation Experiments

The experimental procedure for analyzing the membranes was as follows:

- After heating the membrane to the sealing temperature then cooling to the test temperature, the sweep gas was started at a flow of 20 sccm and an inert feed gas of helium was started at a flow of ~ 50 sccm.
- After allowing the gas flows to equilibrate for 30 minutes, the sweep gas was introduced into the vacuum chamber and the pressure on the ion gauge was set at 1 X 10^{-6} torr.
- The mass spectrometer was started and was allowed to stabilize for ~30 minutes to achieve a stable background for m/z = 40 (argon).
- The feed gas was changed to a mixture of argon and helium. A stable reading for m/z = 40 indicated that there was no leak through either the seal or the membrane, and the argon was shut off.
- After m/z= 2 and m/z =18 were stable, a background reading of the mass spectra was taken.
- Following acquisition of the background spectra, the feed gas stream was changed to the test gas (typically a mixture of hydrogen and helium) and mass spectra data was acquired every 3-5 seconds until a stable reading was obtained.
- After acquiring permeation data at the highest temperature, data was then acquired at each lower test temperature.
- The sample was then heated back to the initial temperature and the feed gas was changed.

The hydrogen permeation flux was calculated using the following equation,

$$J_{H_2} = \frac{F_{He} c_{H_2}}{A} \tag{3-10}$$

where F_{He} is the sweep gas helium flow rate [cm^3 min^{-1} (STP)], cH_2 is the hydrogen concentration (determined using mass spectrometer), and A is the geometric permeation area at the sweep side of the membrane (cm^2). The concentration of hydrogen was determined by subtracting the background m/z =2 value from the stabilized test m/z = 2 value then applying a calibration curve. The calibration curve was determined using helium gas containing small levels of hydrogen (from 10 to 1000 ppm). The hydrogen permeation flux values calculated using equation 3-10 had units of [cc/cm^2-min]. Assuming the ideal gas law, these flux values were also converted to [mol/cm^2-s].

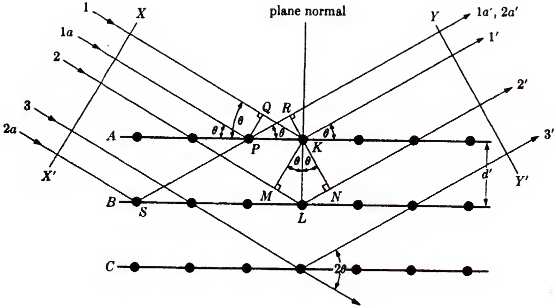

Figure 3-1. X-ray diffraction by a crystal [from ref 74]

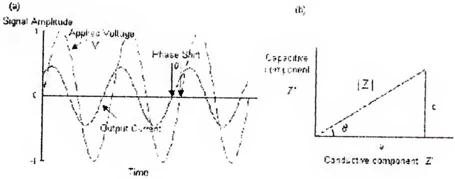

Figure 3-2. (a) Typical current response used to calculate complex impedance and (b) Relationship between capacitive and conductive components of impedance [from ref 70]

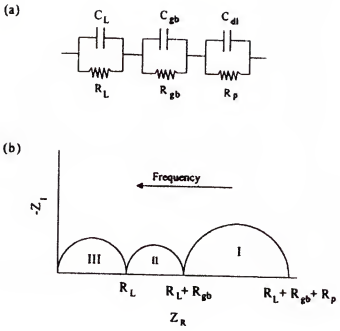

Figure 3-3. Equivalent circuit (a) of an ideal Nyqvist plot with semicircles (b) representing mass transport through the grain interiors (III), mass transports across grain boundaries (II), and mass transport at the electrode/electrolyte interface [from ref 71]

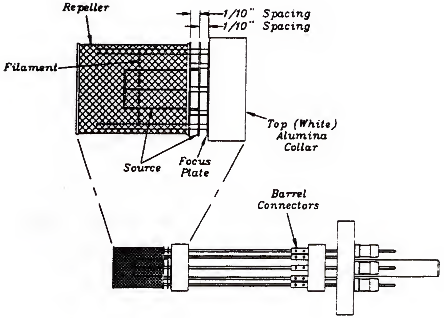

Figure 3-4. Ametek quadrupole mass spectrometer head

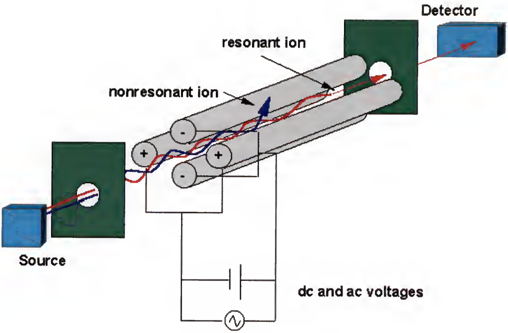

Figure 3-5. Schematic of mass filtering with a quadrupole mass spectrometer [from ref 75]

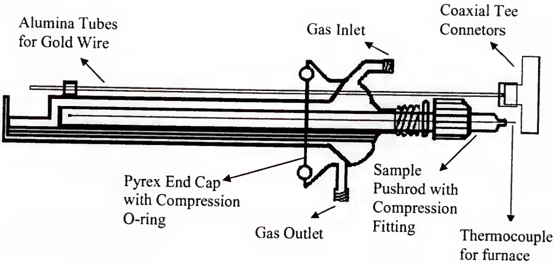
Alumina Tubes for Gold Wire
Gas Inlet
Coaxial Tee Connetors
Pyrex End Cap with Compression O-ring
Sample Pushrod with Compression Fitting
Gas Outlet
Thermocouple for furnace

Figure 3-6. Sample holder for conductivity measurements

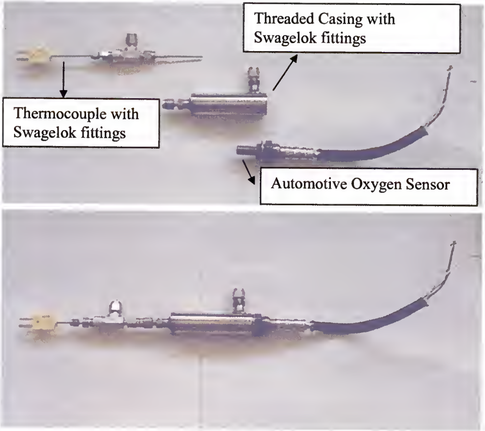
Threaded Casing with Swagelok fittings
Thermocouple with Swagelok fittings
Automotive Oxygen Sensor

Figure 3-7. Oxygen sensor developed for conductivity measurements

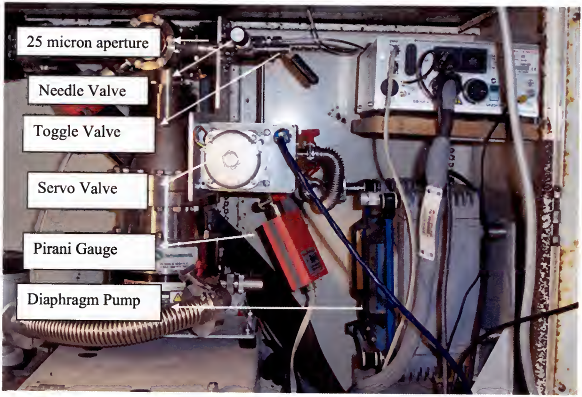

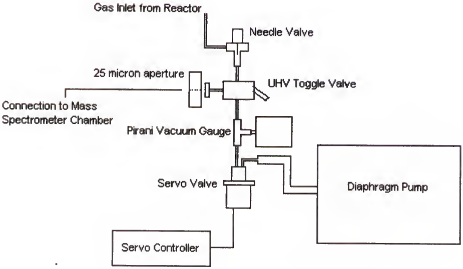

Figure 3-8. Photograph and schematic of gas inlet pumping station

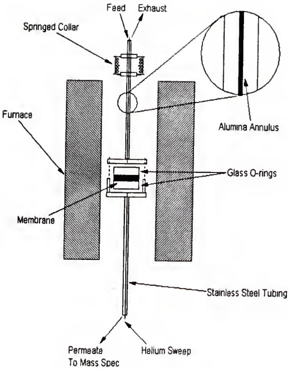

Figure 3-9. Initial stainless steel permeation apparatus

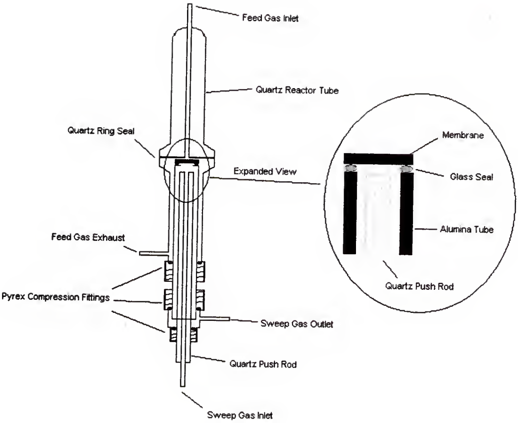

Figure 3-10. Schematic of the quartz/alumina apparatus developed for permeation experiments

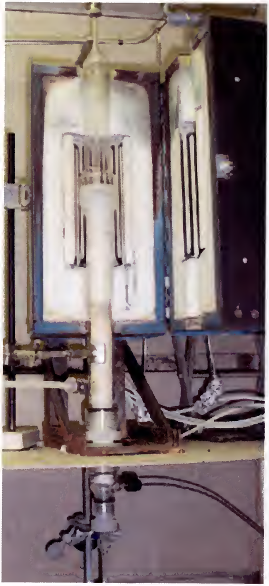

Figure 3-11. Photograph of permeation apparatus which is clamped and loaded into the test furnace

CHAPTER 4
ELECTRICAL CONDUCTIVITY INVESTIGATION OF EUROPIUM-DOPED BARIUM CERATE

4.1 Introduction

The protonic conductivity of barium cerates ($BaCeO_3$) is influenced by the ionic radii of the dopant cation. The most thorough investigation of the effect of ionic radii on protonic conductivity, by Iwahara et al.,[76] demonstrated that $BaCeO_3$ doped with either 20 mol% Y or 20 mol% Gd has the highest conductivity in a hydrogen atmosphere. Stevenson et al. [31] determined that 15 mol% Gd-doped $BaCeO_3$ had a higher conductivity than 20 mol% Gd tested in wet air. The Gd-doped system is an unlikely candidate for use as a single phase hydrogen separation membrane since Bonanos found that below 1000°C Gd-doped $BaCeO_3$ demonstrates insignificant electronic conduction [29]. This lack of electronic conductivity was attributed to the stability of the Ce^{4+} ion in the octahedral environment of the perovskite B-site. Although Gd-doping results in the high protonic conductivity in hydrogen-containing atmospheres, its does not contribute to the electronic conductivity due to its univalent nature. A potential dopant for improving electronic conductivity while maintaining high protonic conductivity is Eu since it has an ionic radii comparable to Gd ($r_{Gd} = 0.94$Å and $r_{Eu} = 0.95$Å) and is multivalent (+2/+3). For this study, the conductivities of 15 mol% Gd-doped and 15 mol% Eu-doped $BaCeO_3$ were measured and compared. Since the conductivities for both materials were comparable, further investigation of Eu-doped $BaCeO_3$ was performed. The conductivities of predominantly single phase $BaCe_{1-x}Eu_xO_{3-\delta}$ (x = 0.05, 0.10, 0.15, 0.20, 0.25) sintered pellets were determined in air, wet nitrogen, and forming gas (4% hydrogen/96% nitrogen).

The total conductivity of a material is equal to the sum of the conductivities of all charge carriers present under a given test condition given by equation 4-1.

$$\sigma = \sum n_i (z_i e)\, \mu_i \qquad (4\text{-}1)$$

where n_i is the concentration and μ_i is the mobility of a charge carrier with a valence of z_i and e is the electronic charge. In each atmosphere studied, a different set of defects contributes to the total conductivity. In forming gas, the external equilibria reaction is:

$$\tfrac{1}{2}\, H_2\,(\text{gas}) + O_o^x \leftrightarrow OH_o^{\cdot} + e' \qquad (4\text{-}2)$$

where the main defects are protons and electrons. In air, the reaction equation is:

$$\tfrac{1}{2}\, O_2\,(\text{gas}) + V_o^{\cdot\cdot} \leftrightarrow O_o^x + 2h^{\cdot} \qquad (4\text{-}3)$$

where the main defects are oxygen vacancies and holes. In wet nitrogen, a potential reaction equation is:

$$H_2O(\text{gas}) + V_o^{\cdot\cdot} + O_o^x \leftrightarrow 2\, OH_o^{\cdot} \qquad (4\text{-}4)$$

where the main defects are oxygen vacancies and protons.

4.2 Experimental Methods

For the initial study, powders of both 15 mol% Gd-doped $BaCeO_3$ and 15 mol% Eu-doped $BaCeO_3$ were prepared by methods comparable to Stevenson et al.[31] This procedure, described in the chapter 3, had three main steps; mixing, first calcination (1100°C), and second calcination (1350°C). Powder x-ray diffraction was performed after each step. The conductivities of samples that were uniaxially pressed, isostatically repressed, then sintered at 1650°C were determined between 450°C and 750°C using A.C.

impedance spectroscopy with the Solartron 1260 frequency response analyzer. Both samples were tested in wet forming gas and wet air.

For the second study, powders of $BaCe_{1-x}Eu_xO_{3-\delta}$ (x = 0.05, 0.1, 0.15, 0.20, 0.25) were prepared by the same method as the initial study. Powder x-ray diffraction was performed on all compounds. The powders were isostatically pressed into bulk pieces and sintered at different temperatures (1450°, 1550°, and 1650°C) for 10 hours. After sintering, SEM samples of each dopant/temperature combination were prepared. The samples were polished using conventional techniques and were etched in dilute nitric acid for ~30-45 seconds to reveal grain boundaries. The total conductivities of the Eu-doped $BaCeO_3$ samples sintered at 1650°C were measured between 450° and 800°C in dry forming gas, dry air, and wet nitrogen.. The conductivity data reported is for temperatures above 450°C. Below 450°C, the grain boundary conductivity can substantially affect the total conductivity. Also, the intended application temperature for these materials is between 600° and 900°C so any low temperature data is extraneous.

4.3 Results

Figure 4-1 illustrates the x-ray diffraction pattern of the 15 mol% Eu-doped $BaCeO_3$ powder after each processing step. Second phases are present after calcining at 1100°C confirming the need for a second calcining step. Predominately single phase powders of 15 mol% Eu-doped $BaCeO_3$ (BCE15O) and of 15 mol% Gd-doped $BaCeO_3$ (BCG15O) were formed after calcining at 1350°C as shown in figure 4-2. These powders had an orthorhombic crystal structure at room temperature.

The total conductivities of BCG15O and BCE15O between 450° and 750°C in wet forming gas and wet air are shown in figure 4-3. In both atmospheres, the BCE15O sample demonstrated higher conductivity over the entire temperature range. The increased conductivity of $BaCeO_3$ doped with 15 mol% Eu supports investigation of other Eu dopant levels to determine the composition with the highest conductivity.

Figure 4-4 shows the x-ray diffraction patterns for 5, 10, 15, 20 and 25 mol% Eu-doped $BaCeO_3$ powders after calcining at 1350°C. All were predominantly single phase. The peaks for all powders are indicative of an orthorhombic phase. The degree of distortion from orthorhombic symmetry increases with increasing dopant content which is expected since Eu^{3+} has a larger ionic radius (0.95 A) than Ce^{4+} (0.87 A).

The SEM micrographs of all dopant/temperature combinations are shown in figure 4-5. The grain size numbers were estimated using the grain count method from ASTM standard E-1382-97. The grain size numbers were used to calculate a linear grain size (in microns) for a more convenient comparison. The estimated grain sizes are shown in table 4-1. The size of the grains increased with sintering temperature indicative of grain coarsening in the final stage of sintering. The grain size also increased with increasing dopant level. At 1550°C, the estimated grain size increased from 1.8 ± 0.1 microns for the 5 mol% Eu sample to 6.0 ± 1.0 microns for 25 mol% Eu. These results are comparable with the work of Park et al. [77] which showed increasing grain size with increasing dopant level for $BaCe_{1-x}Y_xO_3$ ($x = 0.05, 0.10, 0.15, 0.20$) sintered at 1550°C.

Table 4-1. Estimated grain sizes (in microns) for all Eu dopant levels and all three sintering temperatures

Temperature (°C)	Eu Dopant Level				
	5 mol%	10 mol%	15 mol%	20 mol%	25 mol%
1450	1.0 ± 0.1	1.6 ± 0.1	2.0 ± 0.1	3.9 ± 0.2	4.7 ± 0.5
1550	1.8 ± 0.1	3.3 ± 0.1	3.8 ± 0.2	6.0 ± 0.7	6.0 ± 1.0
1650	3.8 ± 0.4	5.8 ± 0.4	6.7 ± 0.3	10.8 ± 0.6	10.8 ± 0.1

The amount of porosity tends to decrease with increasing temperature. Also, it appears that the porosity for the 20 and 25 mol% samples at the lower sintering temperatures is rather large which could be due to excessively agglomerated powders. Densities of individual samples sintered at 1650°C were determined using Archimedes' principle. The densities decreased with increasing dopant level (Table 4-2).

Table 4-2. Bulk densities of $BaCe_{1-x}Eu_xO_{3-\delta}$ bulk samples sintered at 1650°C

Eu dopant level (mol%)	Density (g/cc)	Percent theoretical density (%)
5	6.20	97.5
10	6.17	97.0
15	5.95	93.6
20	5.70	89.6
25	5.69	89.5

The conductivities of the Eu-doped $BaCeO_3$ samples (10-25 mol% Eu), measured in dry forming gas, dry air, and wet nitrogen, exhibit an Arrhenius behavior (figures 4-6 and 4-7). Some representative impedance spectra collected in dry forming gas are shown in appendix A. In all four cases, a similar transition occurred where below 600°C the conductivity in wet nitrogen and dry forming gas was higher while above 700°C the conductivity in dry air was higher. The apparent activation energies in all atmospheres are listed in table 4-3. In dry air, activation energies for all dopants are ~ 0.6 eV which is indicative of p-type electronic conduction.[78] The activation energies in both dry forming gas and wet nitrogen are ~0.35-0.45 eV for all dopant levels which are within the typical range for protonic charge migration.[79-81] These results compare favorably to the work of Slade and Singh on 10 mol% Y-doped $BaCeO_3$ (0.37 eV in moist nitrogen and 0.44 eV in H_2/He).[80]

Table 4-3. Activation energies for conductivity of different Eu dopant levels tested in different atmospheres

	Dry Air	Dry Forming Gas	Wet Nitrogen
	E_a (eV)	E_a (eV)	E_a (eV)
$BaCe_{0.90}Eu_{0.10}O_{3-\delta}$	0.58 ± 0.04	0.35 ± 0.02	0.42 ± 0.01
$BaCe_{0.85}Eu_{0.15}O_{3-\delta}$	0.59 ± 0.03	0.46 ± 0.04	0.38 ± 0.02
$BaCe_{0.80}Eu_{0.20}O_{3-\delta}$	0.63 ± 0.03	0.43 ± 0.04	0.38 ± 0.02
$BaCe_{0.75}Eu_{0.25}O_{3-\delta}$	0.58 ± 0.04	0.39 ± 0.05	0.39 ± 0.02

The composition dependence of conductivity in all atmospheres at 600°C, 700°C, and 800°C is shown in figure 4-8. The conductivity goes through a maximum for 15 mol% Eu in all atmospheres. In dry forming gas, the maximum conductivities were ~0.008 S/cm^2 at 600°C and ~0.024 S/cm^2 at 800°. The curves in dry forming gas show an upward trend at 25 mol% which could be due to increasing electronic conductivity.

4.4 Conclusions

Initial studies showed that the conductivity of Eu-doped $BaCeO_3$ compares favorably to that of Gd-doped $BaCeO_3$ which has one of the highest conductivities in hydrogen-containing atmospheres. Predominantly single phase powders of $BaCe_{1-x}Eu_xO_{3-\delta}$ (x = 0.05, 0.1, 0.15, 0.20, 0.25) were prepared. The effect of dopant level and of temperature on microstructure was investigated. The grain size increased with temperature (2.0 ± 0.1 µm at 1450°C to 6.7 ± 0.3 µm at 1650°C for 15 mol% Eu) and dopant level (3.8 ± 0.4 µm for 5 mol% Eu to 10.8 ± 0.1 µm for 25 mol% Eu at 1650°C). The conductivities of all Eu-doped systems were measured in dry air, dry forming gas, and wet nitrogen. The apparent activation energies in dry air (~0.60 eV) were typical for p-type electronic conduction, while in both dry forming gas and wet nitrogen, the activation energies (0.35-0.45 eV) were consistent with values determined for proton conduction. The 15 mol% Eu-doped $BaCeO_3$ demonstrated the highest conductivity in all atmospheres (0.024 S/cm^2 in dry forming gas at 800°C and was selected for further investigation as a potential material for hydrogen separation membranes.

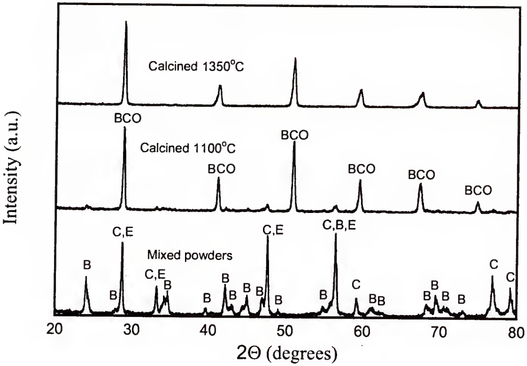

Figure 4-1. X-ray diffraction pattern for $BaCe_{0.85}Eu_{0.15}O_{3-\delta}$ before calcining, after calcining at 1100°C, and after calcining at 1350°C (B=$BaCO_3$, C=CeO_2, E=Eu_2O_3, BCO=barium cerate)

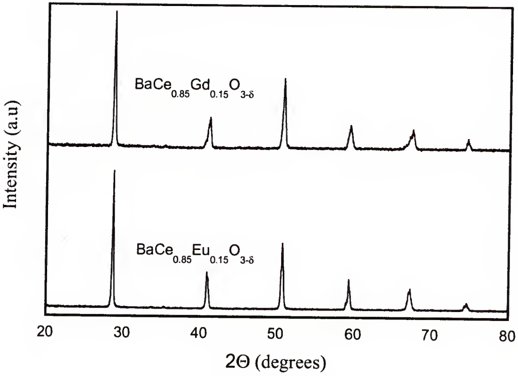

Figure 4-2. X-ray diffraction patterns of single phase $BaCe_{0.85}Gd_{0.85}O_{3-\delta}$ and $BaCe_{0.85}Eu_{0.85}O_{3-\delta}$ after calcining 1350°C

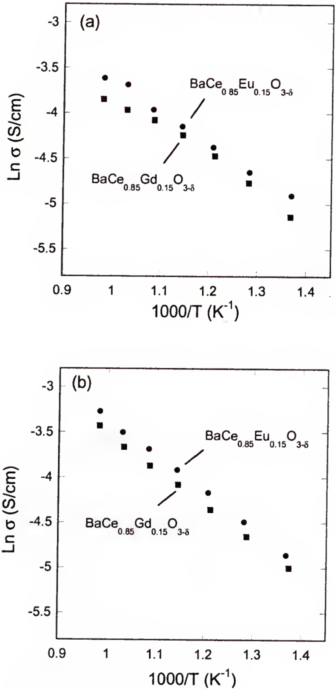

Figure 4-3. Conductivity comparison of $BaCe_{0.85}Gd_{0.15}O_{3-δ}$ and $BaCe_{0.85}Eu_{0.15}O_{3-δ}$ in (a) wet forming gas (4% hydrogen/96% nitrogen) and (b) wet air

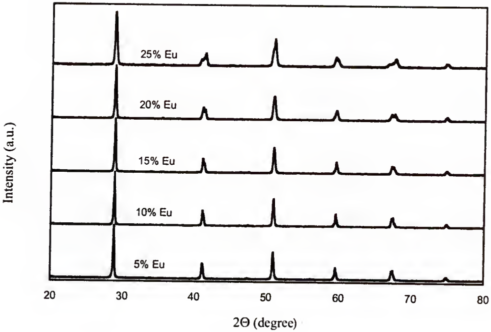

Figure 4-4. X-ray diffraction patterns of $BaCe_{1-x}Eu_xO_{3-\delta}$ (x = 0.05, 0.1, 0.15, 0.20, 0.25) powders after calcining at 1350°C

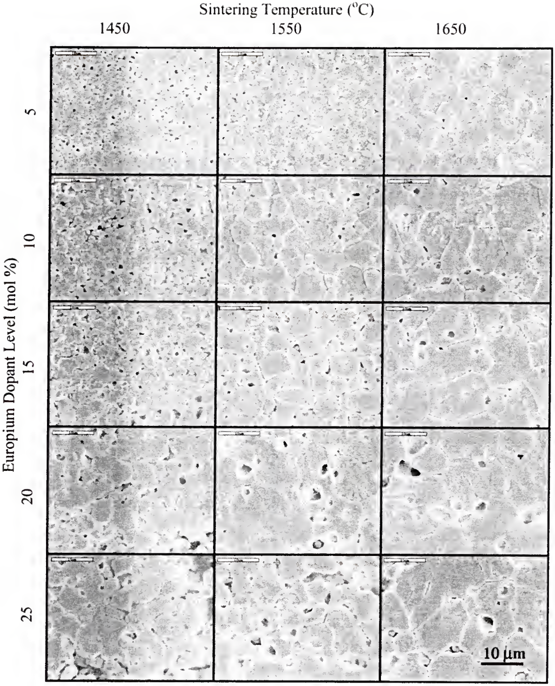

Figure 4-5. SEM micrographs demonstrating the effect of dopant level and temperature (the marker in the upper left of each micrograph is 10 microns)

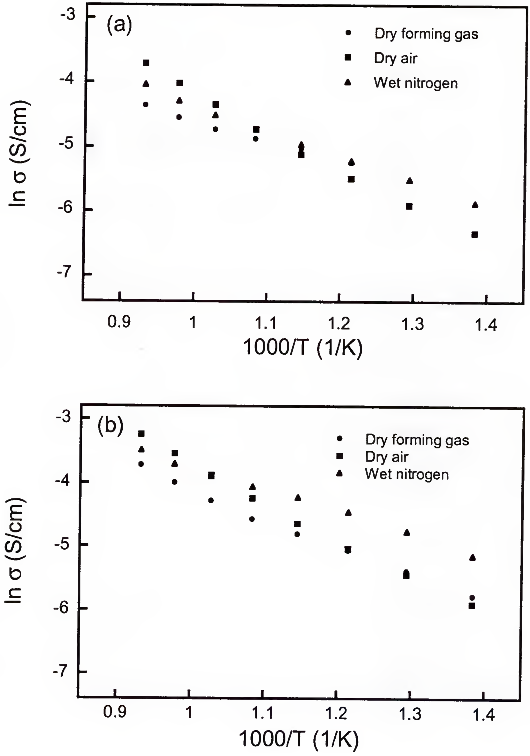

Figure 4-6. Total conductivity for (a) $BaCe_{0.90}Eu_{0.10}O_{3-\delta}$ and (b) $BaCe_{0.85}Eu_{0.15}O_{3-\delta}$ in dry forming gas, oxygen, and wet nitrogen

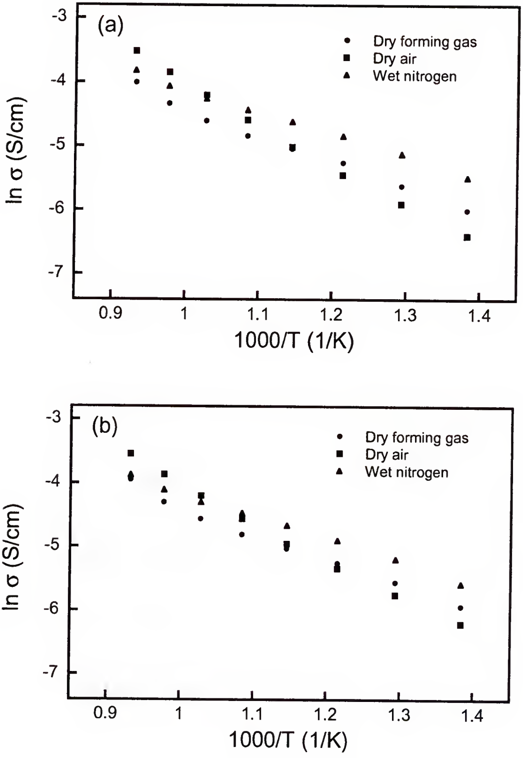

Figure 4-7. Total conductivity for (a) $BaCe_{0.80}Eu_{0.20}O_{3-\delta}$ and (b) $BaCe_{0.75}Eu_{0.25}O_{3-\delta}$ in dry forming gas, oxygen, and wet nitrogen

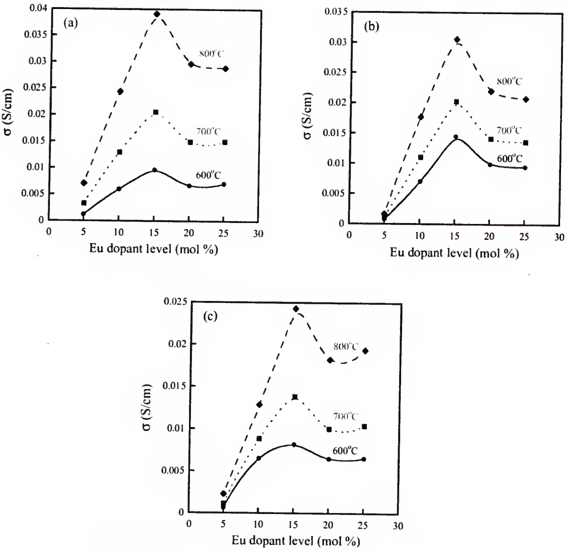

Figure 4-8. Total conductivity as a function of Eu dopant level for $BaCe_{1-x}Eu_xO_{3-\delta}$ in (a) dry air, (b) wet nitrogen, and (c) dry forming gas

CHAPTER 5
ELECTRONIC CONDUCTION OF EUROPIUM-DOPED BARIUM CERATE

5.1 Introduction

In chapter 4, the highest total conductivity for europium-doped barium cerate was determined to occur when doping with 15 mol% europium on the B-site of this ABO_3 perovskite ($BaCe_{0.85}Eu_{0.15}O_{3-\delta}$). This conductivity is the sum of the conductivities of the individual charge carriers. For hydrogen permeation membranes to succeed, the total conductivity of the membrane material must be mixed, consisting of both protonic and electronic components.

5.1.1 Measurement Techniques

The electronic conductivity of mixed-conducting oxides has been examined by techniques such as Hebb-Wagner (H-W) polarization and conductivity as a function of oxygen partial pressure.[29, 82-84] The H-W polarization technique involves using an ion-blocking electrode to block the ionic current allowing for measurement of only the electronic current. By isothermally measuring conductivity as a function of oxygen partial pressure (Po_2), it is possible to separate the Po_2-independent ionic conductivity from the Po_2-dependent p-type and n-type conductivity.

5.1.2 Po_2-dependence of Conductivity

With proton conductors, the Po_2-dependence of conductivity has been a more common technique for analyzing electronic conduction.[29, 83, 84] At low oxygen partial pressures, typically generated using H_2/H_2O or CO/CO_2 mixtures, oxygen ions vacate the lattice resulting in the formation of oxygen vacancies ($V_o^{\cdot\cdot}$) and electrons (e'):

$$O_o^x \rightarrow V_o^{\cdot\cdot} + ½ O_2\,(gas) + 2e' \qquad (5\text{-}1)$$

The equilibrium equation for this reaction yields:

$$n = K_R\,[V_o^{\cdot\cdot}]^{-1/2}\,(Po_2)^{-1/4} \qquad (5\text{-}2)$$

At high oxygen partial pressures, generated by inert gas/oxygen mixtures, the dissolution of oxygen ions results in the formation of electron holes (h·)

$$½ O_2\,(gas) + V_o^{\cdot\cdot} \leftrightarrow O_o^x + 2h \qquad (5\text{-}3)$$

The equilibrium reaction for this reaction yields:

$$p = K_O\,[V_o^{\cdot\cdot}]^{1/2}\,(Po_2)^{1/4} \qquad (5\text{-}4)$$

From equations 5-2 and 5-4, it is evident that the n-type conductivity increases with decreasing oxygen partial pressure and that the p-type conductivity increases with increasing oxygen partial pressure. The general equation applied to the variation of conductivity with oxygen partial pressure:[83-85]

$$\sigma_{total} = A + B\,(Po_2)^{-1/4} + C\,(Po_2)^{1/4} \qquad (5\text{-}5)$$

With equation 5-5, σ_{total} represents the total conductivity, A is the Po_2-independent ionic conductivity, B is the contribution from electrons (n-type conductivity) and C is the contribution from electron holes (p-type conductivity).

Since hydrogen membranes are intended to operate under highly reducing conditions, it is important to analyze the contribution of electrons to the conductivity of proton-conducting oxides. Kosacki and Tuller [83] demonstrated that $SrCe_{0.95}Yb_{0.05}O_3$ exhibits mixed ionic-electronic (n-type) conduction between 600°-1000°C using CO/CO_2 mixtures to obtain low oxygen partial pressures. Phillips et al. [84]obtained similar results for $SrCe_{1-x}Y_xO_{3-\delta}$ (x=0.025-0.20) at 800°C using H_2/H_2O mixtures. Bonanos [29] studied the mixed-conducting properties of $BaCe_{0.9}Gd_{0.1}O_{2.95}$ between 800°-1200°C using

H_2/H_2O mixtures. The onset of n-type electronic conduction for $BaCe_{0.9}Gd_{0.1}O_{2.95}$ did not occur until ~1000°C.

5.1.3 Effect of Hydrogen Atmosphere

In hydrogen atmospheres, protons interact with the oxygen lattice ions:

$$\frac{1}{2} H_2 (gas) + O_o^x \leftrightarrow OH_o^{\cdot} + e' \qquad (5\text{-}6)$$

From this reaction, the electronic conductivity can be expected to increase with protonic conduction resulting in the mixed conduction necessary for hydrogen membranes. Kosacki et al. [35] examined the effect of hydrogen atmosphere on the conductivity of $SrCe_{0.95}Yb_{0.05}O_3$. They determined the contribution of electronic conductivity by measuring conductivity as a function of hydrogen partial pressure at 758K and 1013K. According to their analysis, the electronic conductivity should exhibit a ¼ dependence on hydrogen partial pressure so the data was fit with the following equation where A represents the protonic component and B represents the electronic component:

$$\sigma = A + B\,(P_{H_2})^{1/4} \qquad (5\text{-}7)$$

5.2 Experimental Methods

The conductivity of a $BaCe_{0.85}Eu_{0.15}O_{3-\delta}$ sample as a function of oxygen partial pressure was measured at 600° and 700°C using a.c. impedance spectroscopy. The sample was loaded into the apparatus shown in figure 3-6. For these tests, the temperature was held constant and the test gas varied. The test gases were flowed through a room temperature water bubbler. The test gases were mixtures of helium and oxygen for high partial pressures and hydrogen and helium for low partial pressures. The oxygen sensor was used to measure the oxygen partial pressure of the gas on the outlet side of the apparatus. The sample was equilibrated at each oxygen partial pressure for an hour before a measurement was taken.

The conductivity of a $BaCe_{0.85}Eu_{0.15}O_{3-\delta}$ sample as a function of hydrogen partial pressure was also measured between 600°C and 850°C using a.c. impedance spectroscopy. The hydrogen partial pressure was varied between 0.01 to 1.0 atm using mass flow controllers to maintain the ratio of hydrogen and nitrogen. For these tests the test gas was held constant and the temperature was varied. The sample was equilibrated at 850°C for 12 hours in the test gas before taking the first measurement. The temperature was then lowered to the next test temperature and allowed to equilibrate for 30-60 minutes before taking the next measurement. Some representative spectra are shown in appendix A.

5.3 Results

The $BaCe_{0.85}Eu_{0.15}O_{3-\delta}$ sample exhibited increased conductivity under both low and high oxygen partial pressures at 600° and 700°C as shown in figure 5-1. The data is modeled using equation 5-5 (shown as the dashed lines in figure 5-1). At both temperatures, the conductivity behavior at high oxygen partial pressures confirms hole (p-type) conductivity. At 600°C, the conductivity only slightly increases with decreasing oxygen partial pressures while at 700°C, the increase is substantially higher. The slight increase in conductivity at 600°C indicates an onset temperature for mixed protonic-electronic (n-type) conduction above which hydrogen permeation could be studied. Bonanos [29] demonstrated a similar slight increase in conductivity for $BaCe_{0.9}Gd_{0.1}O_{2.95}$ at 900°C. The n-type electronic transport in both Eu-doped and Gd-doped barium cerate probably occurs via a small polaron hopping mechanism. This small polaron mechanism is the reason for electronic transport in doped and undoped cerium oxide due to the multivalent character of cerium ($Ce^{4+/3+}$).[86] A small polaron is a defect created when an electronic carrier becomes trapped at a given site as a consequence of the displacement of adjacent atoms or ions.[87] The entire defect then migrates by a hopping mechanism. The 300°C difference in onset temperature for Gd-doped and Eu-doped barium cerate samples could result from improved small polaron hopping due to the multivalent character of Eu ($Eu^{3+/2+}$).

In hydrogen atmospheres, the conductivity demonstrated a gradual increase with hydrogen partial pressure as shown in figure 5-2. The dotted curves in figure 5-2 represent the fitting of equation 5-7 to the data. The fitting parameters for both the ionic and n-type electronic components are shown in table 5-1. Both components exhibit Arrhenius behavior with activation energies of 0.61eV for the ionic component and 0.77 eV for the electronic component.

Table 5-1. Fitting parameters from conductivity versus hydrogen partial pressure measured between 600° and 850°C.

Temperature (°C)	A (mS/cm)	B (mS atm$^{-1/4}$/cm)
600	6.0 ± 0.1	0.9 ± 0.1
650	8.3 ± 0.1	1.3 ± 0.2
700	11.7 ± 0.3	2.1 ± 0.4
750	16.0 ± 0.4	3.1 ± 0.6
800	22.0 ± 0.7	4.5 ± 0.9
850	28.0 ± 0.8	6.8 ± 1.0

5.4 Conclusions

The $BaCe_{0.85}Eu_{0.15}O_{3-\delta}$ exhibited electronic conduction at low oxygen partial pressures at both 600° and 700°C. This n-type electronic conduction is necessary for hydrogen permeation. The onset temperature for electronic conduction with Eu-doped barium cerate occurs at 600°C which is 300-400°C lower than with Gd-doped barium cerate. The conductivity of $BaCe_{0.85}Eu_{0.15}O_{3-\delta}$ increases with increasing hydrogen partial pressure.

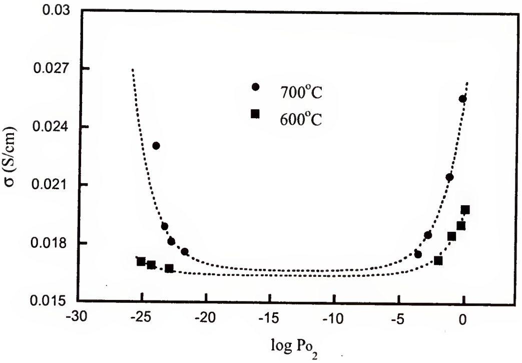

Figure 5-1. Conductivity measured as a function of oxygen partial pressure

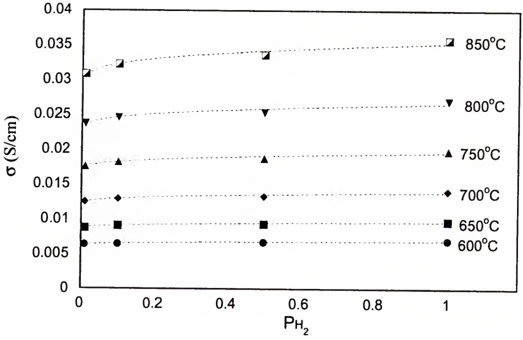

Figure 5-2. Conductivity measured as a function of hydrogen partial pressure

CHAPTER 6
GLASS SEAL DEVELOPMENT

6.1 Introduction

For our permeation studies, the dense, planar ceramic membrane must be sealed to a dense alumina tube at high temperatures (600°-900°C). Ideally, the seal will be hermetic and will not react with the membrane material. Limited information on high temperature seals has been reported by previous researchers. This chapter will discuss the different seals used by other researchers, the important parameters when developing a glass seal, the types of sealing materials tested in our research, and the final seal composition used for permeation tests.

6.1.1 Types of High Temperature Seals

The types of seal used are dependent on the membrane material and on the support material. Three types of potential seals include solders, precious metals, and glasses. Soldering or brazing consists of joining a ceramic membrane to a metal support using alloys such as Ag-Cu-Ti, Au-Ti-Ni, Ag-Cu, or some Cr-based alloys.[88-90] The alloy is heated to above its melting temperature to form a permanent seal and lowered for testing. The key issues concerning this type of seal are selecting an alloy with good chemical compatibility with both the membrane and the metal support and finding a metal alloy which will sufficiently wet the ceramic membrane.

Sealing with precious metals (silver or gold) can occur in two ways -- precious metal pastes or rings.[91-96] The main advantage of silver and gold is chemical inertness at high temperatures. The pastes or rings fill the gap between a planar or tubular membrane and the support tube, and a compressive force is necessary to form a hermetic seal. Thermal stresses can result from differences in thermal expansion between the precious metal, the membrane, and the support. These thermal stresses combined with the compressive force can result in membrane failure during thermal cycling.

The last type of seal involves joining the membrane and the support with a glass or glass-ceramic.[97-100] The glass ring or paste softens at higher temperatures and flows filling the gap between the membrane and the support. The glass then solidifies on cooling down to the permeation test temperature range. The glass-based seals tend to have better wetting properties and thermal expansion compatibility with both the ceramic membrane and the support material than precious metals. The main disadvantage with using glass sealants is the potential for chemical reaction between the glass and the membrane.

6.1.2 Membrane-to-Support Sealing Configurations

Different membrane-to-tubular support glass sealing configurations for planar membranes are possible (Figure 6-1). In the vertical furnace used for testing, configurations in figure 6-1a and 6-1b use gravitational force to seal the membrane to the softened glass. The main difference between the two configurations is edge sealing of the membrane. The configuration in figure 6-1a constrains the glass sealing material resulting in consistent edge sealing. This constraint of the glass might also result in increased radial stress on the membrane upon glass solidification. Although edge sealing using the configuration in figure 6-1b is not guaranteed, it will occur with control of the membrane thickness and the amount of glass sealant. The configuration in figure 6-1c requires more compressive loading of the membrane than the other configurations.

While sealing can be improved, the probability of membrane failure increases with this compressive load.

6.1.3 Glass Seal Properties

When using the sealing configuration in figure 6-1b, the important properties to consider with the glass seal include the softening point, the wettability, the chemical reactivity, the thermal expansion behavior, and the glass transition temperature.[101, 102] Upon heating, the glass should soften before or near the highest testing temperature. Above the softening point, the viscosity of the glass must be low enough so the glass wets both the membrane and the support while also allowing the membrane to settle sealing the edges. The glass must be chemically inert at the highest temperatures.

The chemical reactivity of the glass can affect the seal in three ways: (1) the glass can react with the support; (2) the glass can react with the sealing surface of the membrane; (3) the glass can affect the membrane surface and possibly the bulk of the membrane. Reactions with the support and the sealing surface might limit the testing life of the seal within the permeation temperature range and might also decrease the size of this temperature range. The most crucial reaction can occur between the glass seal and the testing surface and/or the bulk of the membrane. Reactions with the surface or the bulk can dramatically affect the response of the membrane.

The last two properties, the thermal expansion behavior and the glass transition temperature, are most important when cooling the sealed membrane structure. As the seal cools, it becomes more viscous eventually forming a rigid structure. Thermal stresses develop on cooling between the seal and the membrane as well as the seal and the support. The importance of the glass thermal expansion coefficient (TCE) depends on the nature of the seal during operating temperatures. Since the glass may behave as a viscous fluid or a solid during testing, the TCE of the glass is only important when the glass has solidified. If the membrane and the support materials have comparable thermal coefficients of expansion, the glass seal material should have a similar TCE. If there are differences in the TCEs of the membrane and the support material, the TCE of the glass should be between these values. The degree of difference should be minimized to increase the temperature range for testing. Below the glass transition temperature (T_g), the stress within the glass is significant, eventually resulting in failure of the seal. Therefore, the T_g of the glass seal should be below the lowest permeation test temperature.

6.2 Experimental Methods

Glass seal development was divided into three phases. Phase one involved investigation of some common glasses, a borosilicate and an aluminosilicate, which had been used with a compressive reactor design in early experiments. During phase two, glasses recommended by glass supply companies were analyzed. In phase three, glass prepared according to research done at Argonne National Laboratory was studied. The list of sealing glasses studied in phase one and two is shown in table 6-1 along with their suppliers and major components.

Table 6-1. Sealing glass names, suppliers, and main components which were studied during phase one and phase two

Glass Name	Glass Supplier	Components
KG-33	Kimble Glass	SiO_2, B_2O_3, Na_2O, Al_2O_3
EZ-1	Kimble Glass	SiO_2, Al_2O_3
Elan 63	Elan Technology	SiO_2, BaO, K_2O, Na_2O, Li_2O, Al_2O_3
SCC-5	SEM-COM Company	PbO, B_2O_3, ZnO, CuO

The sealing glasses were either in a ring form or in a paste form. The glass pastes were prepared using glass powders combined with ethylene glycol as a binder and isopropanol as a dispersant. The sealing tests were performed by loading a 15 mol% Eu-doped barium cerate membrane onto the glass ring or paste which is atop the alumina support tube. After securing the alumina tube in the permeation apparatus and loading the apparatus into the vertical tube furnace, the temperature was raised to the expected sealing temperature. During heating, helium was flowed on the sweep side of the membrane and argon was flowed on the feed side. The argon level (m/e = 40) in the helium sweep gas was monitored using the mass spectrometer. A dramatic decrease in argon level would indicate a potential good seal. The temperature was then slightly decreased, and the argon feed gas was switched to helium. If the argon level remained constant, the sample was sealed. The temperature range of the seal was investigated by cooling the membrane while flowing argon feed gas and monitoring the argon level in the sweep. After cooling to room temperature, samples were analyzed for wettability of the sealing glass on the membrane, wettability of the sealing glass on the alumina support, and reactivity between the seal and the membrane. The wettabilities were determined by visual inspection while the reactivity was examined using energy dispersive x-ray spectroscopy (EDS).

6.3 Results

6.3.1 Phase One Results

The KG-33 borosilicate glass was tested in a ring form and as a high-viscosity paste. The KG-33 ring and paste were both heated to 900°C and held for one hour. In both cases, the membrane was not sealed. Both seals were reheated to 950°C and the membranes never sealed. In the case of the KG-33 ring, the glass did wet the membrane but failed to wet the alumina tube. The KG-33 paste also wet the membrane but did not wet the alumina tube, had poor flow characteristics, and did not completely seal around the membrane surface.

Even though the EZ-1 aluminosilicate had a higher softening temperature (912°C) than the KG-33 (827°C), it was tested as a potential seal. A membrane was tested using a ring of EZ-1. It was heated to 1000°C and the membrane never sealed. The EZ-1 did not wet either the membrane or the alumina support.

6.3.2 Phase Two Results

The Elan 63 was tested in three forms – a low viscosity paste, a high viscosity paste, and a high viscosity paste with 10 wt% barium cerate powder. The low viscosity paste was heated up to ~850°C and a seal could not be achieved. The Elan 63 had coated the alumina tube, the quartz push rod, and the inside of the quartz tube as well as a thin layer on the membrane. The high viscosity paste was also heated to ~850°C resulting in a temporary seal which was quickly lost when the membrane was cooled below 850°C. Similar to the low viscosity paste, the high viscosity paste also coated the inside of the quartz tube. The low softening temperature (625°C) of the Elan 63 was more than likely the cause of the damage to the quartz tube. To improve the flow characteristics of the seal, the Elan 63 was mixed with 10 wt% barium cerate powder. This high viscosity paste and membrane were heated to >850°C and tested starting at 850°C. The combination of Elan 63 and barium cerate powder resulted in a good seal which was lost below 700°C. The membrane could not be resealed when heated above 850°C. Upon removal from the apparatus, the membrane had a white discolored surface which before testing was dark green. EDS analysis of this surface showed traces of silicon which is the major component of the Elan 63 glass. The EDS spectra comparing an untested membrane surface to the Elan 63 tested surface are in figure 6-2. The peak intensity for cerium for the tested membrane was lower than for the untested membrane indicating other changes to the membrane surface.

Consultations with different companies produced very limited results. A technician at SEM-COM Company recommended trying their SCC-5 glass used to seal to alumina. The SCC-5 formed at seal ~725°C. The seal failed at ~650°C. After removing the membrane from the alumina support, the permeation surface appeared to have a shimmer that was not present before testing. EDS of this surface, shown in figure 6-3, revealed the presence of lead on the test surface eliminating the application of SCC-5 as a sealing material.

6.3.3 Phase Three Results

Ley et al. [102] developed some glass and glass-ceramic sealants for solid oxide fuel cells. Guan et al. [62, 98] used one of the glasses (ANL Mat43) to fix barium cerate and strontium cerate samples to alumina tubes for transference number tests. They did not discuss a method used to determine if the samples were hermetically sealed. ANL Mat43 was selected as a potential seal material for our barium cerate membranes. The composition of the glass is shown in Table 6-2.

Table 6-2. Composition of ANL Mat43 (mol%)

SrO	La_2O_3	Al_2O_3	B_2O_3	SiO_2
41.76	3.74	16.27	27.01	11.23

The boron oxide is the primary glass former which aids in obtaining a low T_g. The strontium oxide is added to increase the CTE, while lanthanum oxide is used to control the viscosity. The addition of alumina retards crystallization of strontium borate and other crystalline phases. The silica increases the glass-forming composition range.

The powders of each component were weighed and were mixed in a polyethylene jar with zirconia media and ethanol for 10 hours. The glass batch was heated in a platinum crucible to 1400°C using a Deltech bottom loading furnace. The glass melt was poured into a large Pyrex beaker filled with water. The glass was then ground using a synthetic sapphire (diamonite) mortar and pestle.

The ANL Mat 43 glass did seal the membrane at >850°C but the seal failed at ~650°C. Subsequent sealing attempts produced inconsistent results. The inability to produce a good seal led to modification of the sealing process. All previous sealing attempts with glass powders were single step processes -- the glass paste and the membrane were heated together. The three main disadvantages of this process were difficulty loading the alumina tube holding the glass powder and the membrane, inconsistent seals, and poor edge sealing of the membrane. A two-step process was employed for the remaining sealants to avoid these problems. For the first step, the glass paste was melted to the top of the alumina tube. The second step involved loading the membrane and heating to the sealing temperature.

The final two sealants were prepared from a mixture of ANL Mat43 glass and barium cerate powder. The glass frit and barium cerate powder were mixed with isopropanol in a mortar and pestle followed by the addition of ethylene glycol. Some of the isopropanol was evaporated off until the mixture was relatively viscous. The top of the alumina tube was then lined with tape to create a ~2.0 mm lip and a rubber stopper was inserted in the top of the tube. The viscous paste was added to fill the gap between the tape and the stopper. After the paste had partially dried, the tape and the stopper were removed from the tube leaving a thick, relatively uniform layer of sealant. The alumina tube was inserted into the vertical furnace and heated to 350°C to burn-off the organics then heated to 950°-980°C. The sealant was inspected at temperature by cracking open the furnace. After the glass had started to melt, the tube was held at temperature for 1 hour then cooled to room temperature. The glass sealant was then polished to create a flat surface to attach the membrane.

The first ANL Mat43 composite seal contained 25 wt% barium cerate doped with 15 mol% europium (BCE15O). The first stage of seal preparation was completed at 950°C. After attaching the membrane and loading the alumina tube into the quartz reactor, the entire apparatus was inserted into the furnace and heated to 890°C. After holding for 30 minutes, the temperature was lowered to 850°C for testing. The first run of this sealant failed to produce a good seal. A second attempt produced a good seal which failed around 675°C. EDS analysis of the membrane after sealing indicated no noticeable change in surface composition as shown in figure 6-4.

The second and final composite seal included 30 wt% BCE15O. The glass sealant was melted at 975°C after holding for ~1 hour. In the second step, the membranes typically sealed at ~875°C after a 30 minute dwell. The first membrane was cycled between 650°C and 850°C daily for 16 days without failure. This final seal composition and procedure was used for all membrane testing. The results of all three phases of seal development are summarized in Table 6-3.

6.4 Conclusions

When investigating glasses to use for membrane sealing, some important properties to consider are the coefficient of thermal expansion, the softening temperature, and the glass transition temperature. The glass sealant must wet both the membrane and the support tube without reacting with the membrane surface. A variety of commercial glasses were investigated. The borosilicate and aluminosilicate failed to seal the barium cerate membranes to the alumina support due to high softening temperatures. Two other glasses, Elan 63 and SEM-COM SCC-5, sealed the membranes at 850°C and 725°C respectively, but they also reacted with the surfaces of the membranes. The glass sealant selected for membrane testing was based on ANL Mat 43 (a glass developed at Argonne National Laboratory). The glass was mixed with 30 wt % barium cerate powder and used to seal membranes using a two-step process. Membranes could be analyzed between 650°C and 850°C with this sealant.

Table 6-3. Glass seal development summary

Glass Type	Glass Form	Results
KG-33 borosilicate	Ring	Poor sealing due to low wettability of alumina
KG-33 borosilicate	High viscosity paste	Poor sealing due to poor glass flow
EZ-1 aluminosilicate	Ring	No sealing to due high softening point of glass (912°C)
Elan 63	Low viscosity paste	Poor sealing due to glass coating of alumina tube and quartz reactor
Elan 63	High viscosity paste	Occasional seal (quickly lost on cool down)/glass coated quartz reactor
Elan 63 + 10 wt% BCE15O	High viscosity paste	Seal achieved >850°C/failed at 700°C. Silica contaminated membrane surface.
SEM-COM SCC-5	High viscosity paste	Seal achieved ~725°C/failed at 650°C. Pb from glass contaminated the membrane
ANL Material 43	High viscosity paste	Occasional sealing >850°C/failed <650°C
ANL 43 + 25 wt% BCE15O	High viscosity paste	Occasional sealing >890°C/failed ~625-675°C
ANL 43 + 30 wt% BCE15O	High viscosity paste	Sealed ~875°C and cycled between 650-850°C without failure (16 days)

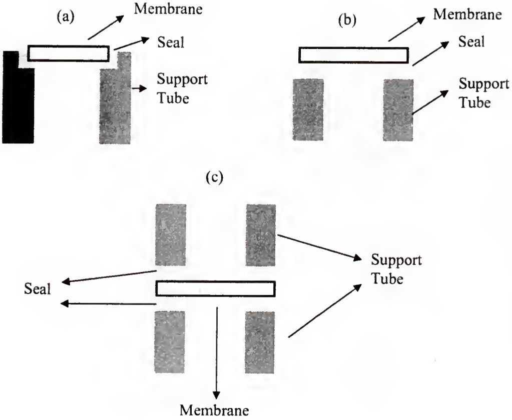

Figure 6-1. Potential membrane-to-tubular support glass sealing configurations: (a) constrained gravitational sealing. (b) gravitational sealing, and (c) compressive sealing.

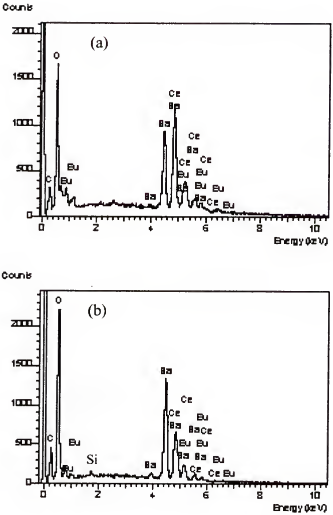

Figure 6-2. Energy dispersive x-ray spectra of (a) an untested membrane surface and (b) a membrane surface after sealing with Elan 63 glass with 10 wt% barium cerate

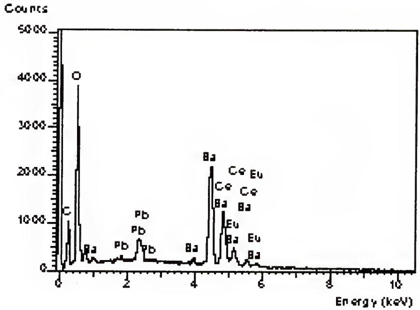

Figure 6-3. Energy dispersive x-ray spectrum of membrane sealed with SEM-COM SCC-5 showing Pb surface contamination

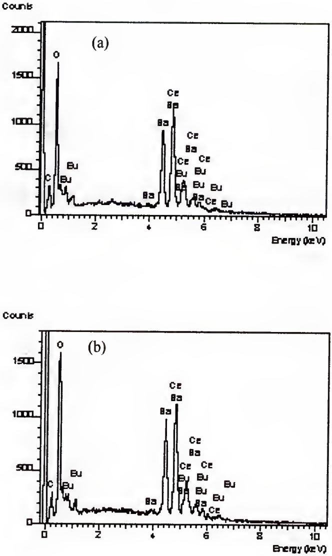

Figure 6-4. Energy dispersive x-ray spectra of (a) an untested membrane surface and (b) a membrane surface after sealing with ANL Mat43 glass with 25 wt% barium cerate

CHAPTER 7

HYDROGEN PERMEATION OF EUROPIUM-DOPED BARIUM CERATE

7.1 Introduction

Dense ceramic membranes are receiving increasing interest for potential applications in hydrogen separation. This interest stems from the advances in mixed-conducting oxygen permeation membranes used to extract oxygen from air or to produce synthesis gas (CO + H_2) from natural gas. Mixed protonic-electronic conducting membranes could be used to extract pure hydrogen from synthesis gas or in other dehydrogenation or hydrogen purification processes.

Hydrogen permeation membranes require high selectivity for hydrogen and high protonic conductivity. For continuous operation without external circuitry, a charge balancing electronic flux is necessary. The majority of research on high temperature protonic conductors has focused on perovskite-type oxides such as $SrCeO_3$, $BaCeO_3$, $SrZrO_3$, and $Ba_3Ca_{1.18}Nb_{1.82}O_{3-\delta}$. The protonic conductivity of these systems increases in the following order between 600° to 800°C: $BaCeO_3 > Ba_3Ca_{1.18}Nb_{1.82}O_{3-\delta} > SrCeO_3 >> SrZrO_3$.[42] Complex perovskites, such as $Ba_3Ca_{1.18}Nb_{1.82}O_{3-\delta}$ do not demonstrate electronic conduction in highly reducing atmospheres limiting there application in hydrogen separation.[45] The low protonic conductivity of doped $SrZrO_3$ compared to $SrCeO_3$ and $BaCeO_3$ minimizes its application as a membrane material.[30, 103] Kosacki and Tuller [83] found that $SrCe_{0.95}Yb_{0.05}O_{3-\delta}$ demonstrates electronic conduction in reducing atmospheres above 600°C indicating possible application for hydrogen separation.

Bonanos [29] showed that $BaCe_{0.80}Gd_{0.20}O_{3-\delta}$ does not demonstrate n-type electronic conduction until above 1000°C. But as shown in chapter 5, $BaCe_{0.85}Eu_{0.15}O_{3-\delta}$ shows the onset of n-type electronic conduction above 600°C similar to $SrCe_{0.95}Yb_{0.05}O_{3-\delta}$ so its hydrogen permeation properties should be investigated.

7.1.1 Hydrogen Permeation

Few papers report hydrogen permeation results for perovskite oxides. Until now, the limited hydrogen permeation studies have focused on doped $SrCeO_3$.[63-65, 104] The protonic conductivity of $BaCeO_3$ is known to be higher than that of $SrCeO_3$, but membrane researchers, such as Qi et al., [63] were concerned with the high conductivity of $BaCeO_3$ in oxygen-containing atmospheres. The hydrogen membranes are intended to operate in low oxygen partial pressure conditions so research in this area should focus on the high protonic conductivity of $BaCeO_3$.

Although there is limited experimental data on hydrogen permeation, there are a number of papers which discuss hydrogen permeation modeling of mixed conductors.[105-107] Norby and Larring [105] developed a model based on conventional transport equations which took the form of the Wagner equation and applied the model to different defect species dominated cases. The model of Tan et al. [106] requires known values for many equilibrium constants and diffusivities which have not been determined for most perovskite compounds. Li and Iglesia [107] developed a rigorous mass transfer model using non-equilibrium thermodynamics which they acknowledge ignores surface kinetics which can be included with advances in proton mixed-conducting membranes. Song et al.[108] developed a numerical model of hydrogen permeation under chemical potential gradients which is based on chemical diffusion theory. Before applying any of these models, it is necessary to understand what affects hydrogen permeation through a particular membrane system.

The driving force for hydrogen transport through the membrane is the difference in hydrogen activity between the feed gas side and the sweep gas (permeate) side. The driving force decreases across the membrane due to limited bulk diffusion of protons and potentially due to non-ideal electrochemical processes at both membrane surfaces. An example of driving force difference across a membrane is illustrated in figure 7-1. This figure has exaggerated surface layers and is drawn assuming linear kinetics at the surfaces and across the membrane. Driving force limitations due to bulk diffusion can be minimized by decreasing the membrane thickness. If hydrogen surface kinetics limit performance, then surface modification is necessary to optimize hydrogen permeation. Possible surface modifications include changing the surface morphology of the membrane or adding a porous catalytic surface layer.

7.1.2 Bulk Diffusion

The fundamental approach of Bouwmeester and Burggraaf for oxygen permeation membranes offers a potential method for describing hydrogen permeation.[67] When the effect of interfacial hydrogen reactions are ignored, the hydrogen flux is governed by the bulk diffusion of hydrogen which can be described by a modified Wagner equation,

$$J_{H_2} = \frac{RT}{2^2 F^2 L} \int_{\ln P'_{H_2}}^{\ln P''_{H_2}} t_{el} \sigma_{ion} d \ln P_{H_2} \tag{7-1}$$

Here J_{H_2} is the hydrogen permeation flux, σ_{ion} is the ionic conductivity, t_{el} is the electronic transference number, L is the membrane thickness, and P_{H_2}'' and P_{H_2}' are the hydrogen partial pressures at the high (feed) and low (sweep) pressure sides of the membrane, respectively. The other parameters have their usual meaning. Wagner's theory assumes that rapid equilibration occurs at the gas phase boundaries and that local thermodynamic equilibrium for internal defect reactions is not affected by mass transport.

When analyzing mixed conductors for oxygen membranes, the electronic transference number is assumed to be predominate ($t_{el} \approx 1$). Therefore, integration of equation 7-1 extends only over σ_{ion}. This cannot be assumed for proton mixed conductors. Differentiating equation 7-1 with respect to ln PH_2'' gives,

$$\left(\frac{\partial J_{H_2}}{\partial \ln P_{H_2}''}\right)_{P_{H_2}'} = t_{el}\sigma_{ion} \bullet \frac{RT}{2^2 F^2 L} \tag{7-2}$$

$$t_{el}\sigma_{ion} = \frac{\sigma_{H^+}\sigma_{el}}{\sigma_{H^+} + \sigma_{el}} = \sigma_{amb} \tag{7-3}$$

Here, σ_{H+} is the protonic conductivity and σ_{amb} is the ambipolar conductivity. According to equation 7-2, the ambipolar conductivity at a given PH_2'' can be obtained from the slope of the JH_2 versus ln PH_2'' at that PH_2'' as long as PH_2' is kept constant.

7.1.3 Mixed Controlled Permeation

Surface reactions may exert partial control over hydrogen transport kinetics. The extent of control may vary with membrane thickness, temperature, and hydrogen partial pressure gradient across the membrane. Bouwmeester and Burggraaf also discussed the concept of characteristic membrane thickness (L_c) which represents a transition point from predominant bulk diffusion control to surface kinetic control.[67] For a variety of oxygen membranes reviewed, the L_c, calculated from diffusion and surface exchange coefficients, varied from 20 to 3000 μm. The L_c is not an intrinsic material property and is dependent on sample preparation. As shown in figure 7-1, the total chemical potential difference $\Delta\mu_{H2}^{total}$ is distributed across the membrane and the rate determining step will account for the largest proportion. For simplified analysis, the transport equations for bulk diffusion and for surface exchange are linearized. This assumption allows for the hydrogen permeation flux to be written as,

$$J_{H_2} = \frac{1}{1+(2L_c/L)} \frac{\overline{\sigma_{amb}}}{2^2F^2} \frac{\Delta\mu_{H_2}^{total}}{L} \tag{7-4}$$

where σ_{amb} is the mean value of the ambipolar conductivity over the applied hydrogen pressure gradient. The characteristic thickness can be defined as

$$L_c = \frac{RT}{2^2F^2} \frac{\overline{\sigma_{amb}}}{j_{ex}^{H}} \tag{7-5}$$

where j_{ex}^{H} (mol H_2 $cm^{-2}s^{-1}$) is the balanced exchange rate at the gas-solid interface without hydrogen potential gradients. The diffusional flux of hydrogen in equation 7-4 is essentially the flux from the Wagner equation reduced by $(1 + (2L_c/L))^{-1}$. The $2L_c$ accounts for the two interfaces and assumes identical properties at both surfaces.

The effect of membrane thickness of hydrogen flux can be assessed by applying equation 7-4 (Figure 7-2). When $L \gg L_c$, the hydrogen flux will be inversely proportional to L^{γ} with $\gamma=1$, which agrees with the Wagner equation. With decreasing membrane thickness, the hydrogen flux becomes partially governed by surface exchange kinetics with deviations from the inverse relationship with L ($0<\gamma<1$). As γ decreases, the extent of control by surface kinetics increases. The value of γ, at a given L, corresponds to the negative slope in the double logarithmic plot of hydrogen flux versus membrane thickness at that L. Equation 7-4 neglects material parameter changes due the hydrogen pressure gradient and typically applies to small P_{H_2} gradients.

Assuming that electronic conduction is predominating in the membranes studied, the equation for the characteristic thickness can be simplified to:

$$L_c = D^* / k_s \tag{7-6}$$

where D^* is the tracer diffusion coefficient and k_s is the surface exchange coefficient. The D^* is a material parameter which is constrained by experimental conditions. Under these experimental conditions, fabrication of membranes below L_c will result in a minimal increase in hydrogen flux unless the value of k_s can be increased.

7.1.4 Surface Modification

Although modifying the surface morphology could enhance permeation by improving k_s, increasing the gas phase reaction area with a porous catalytic layer is a more viable method of improving permeation properties. Kharton et al. [109] examined the effect of surface modification of $La_{0.3}Sr_{0.7}CoO_3$ (LSCO) on oxygen permeation by applying various porous surface layers. They found that applying porous layers of LSCO on the surface of the LSCO membrane resulted in the most significant improvement. Similar results were shown by Teraoka et al [92] for various $La_xSr_{1-x}Co_{1-x}Fe_xO_{3-\delta}$ oxygen membranes. In these cases, the porous oxide layers have significant electronic conduction. While $BaCe_{0.85}Eu_{0.15}O_{3-\delta}$ demonstrates improved electronic conduction, the electronic conduction is not as high as in compounds used for oxygen separation membranes. Therefore, porous layers of platinum, which is known to chemically dissociate molecular hydrogen, might provide a better response with $BaCe_{0.85}Eu_{0.15}O_{3-\delta}$ membranes.

7.1.5 A:B Site Stoichiometry

Varying the A:B site stoichiometry of $BaCe_{0.85}Eu_{0.15}O_{3-\delta}$ membranes could have a positive effect on hydrogen permeation. Poulsen calculated that varying the A:B stoichiometry (both A site excess up to 1.04 and deficient down to 0.96) for doped $SrCeO_3$ results in an increase in proton concentration.[110] Shima and Haile investigated the effect of a varying the A:B stoichiometry (from 0.96 to 1.04) on properties of Gd-doped and undoped $BaCeO_3$ [111] For the doped system, they found that the total conductivities in a hydrogen-containing atmosphere were comparable for A:B ratios of 0.96-1.04. Ma et al. [112] showed that Ba deficient (A:B = 0.95) Y-doped $BaCeO_3$ demonstrated the highest conductivity in hydrogen among compounds with A:B between 0.8 and 1.2. The Ba deficient compounds also were more chemically stable than Ba excess samples. The same effect of A:B site stoichiometry on chemical stability was demonstrated by Sharova and Gorelov for Nd-doped $BaCeO_3$ [113]

7.2 Experimental Methods

The membranes were prepared from pressed $BaCe_{0.85}Eu_{0.15}O_{3-\delta}$ powders which were sintered at 1650°C. Each membrane was polished to size using SiC paper with the final polish using 600 grit paper. The final thicknesses were 0.75, 1.0, and 2.0 mm, and all membranes had diameters of ~24 mm. The glass seal, discussed in chapter 6, was tested for hydrogen diffusion by using a dense alumina disc (Coorstek #65631) as the membranes. After sealing the alumina disc, hydrogen feed gas was flowed and the helium sweep gas was analyzed for an increase in m/z=2. The m/z=2 peak remained stable over a 12 hour test indicating no hydrogen diffusion through the glass seal.

Therefore, if the membrane edges are properly sealed then all hydrogen detected during testing will result from permeation through the membrane.

Hydrogen permeation measurements were performed in the temperature range of 650°-850°C. The membranes were sealed at 875°C then cooled to 850°C for testing. The membranes were tested following the procedure described in chapter 3. The test gases used were hydrogen/helium mixtures with hydrogen partial pressures of 0.1, 0.5, and 0.9 atm. The test gases were controlled at 50 sccm. The initial spectra would take from 2 to 6 hours to achieve a stable m/z=2 reading. The temperature was then decreased to the next test temperature, and the spectra stabilized (typically from 1 to 2 hours). The process was repeated for each test temperature. After testing at 650°C, the hydrogen was shut off and the membrane was reheated to 850°C for testing at the next hydrogen partial pressure.

Surface modification was investigated by applying a layer of platinum paste (Englehard 6926) to both surfaces of a 1.0 mm thick $BaCe_{0.85}Eu_{0.15}O_{3-\delta}$ membrane. The paste was sintered at 1000°C for 30 minutes. The porosity of the platinum layers was confirmed using SEM.

Powders with the compositions $Ba_{0.99}Ce_{0.85}Eu_{0.15}O_{3-\delta}$ and $Ba_{1.01}Ce_{0.85}Eu_{0.15}O_{3-\delta}$ were prepared using the same procedure as $BaCe_{0.85}Eu_{0.15}O_{3-\delta}$ powder. X-ray diffraction of the A:B site modified powders calcined at 1350°C confirmed they were predominantly single phase. Membranes made from the modified powders were sintered at 1650°C and had densities >92% theoretical, thicknesses of 1.0 mm, and diameters of ~24 mm.

Membranes with the composition $BaCe_{0.85}M_{0.15}O_{3-\delta}$ (M= Eu, Sm, and Yb) were prepared from single phase powders. The 1.00 mm thick membranes were sintered at

1650°C. Two layers of platinum paste were applied to both sides of each membrane and partially sintered at 1000°C. These membranes were tested from 700° to 850°C under feed-side hydrogen partial pressures of 0.01, 0.1, 0.5, and 1.0 atm.

7.3 Results

7.3.1 Temperature Dependence

The hydrogen permeation flux through $BaCe_{0.85}Eu_{0.15}O_{3-\delta}$ membranes under different feed-side hydrogen partial pressures and with different thicknesses exhibited Arrhenius behavior as shown in Figure 7-3. The difference in activation energies, shown in table 7-1, for the 0.75 mm membrane and the 2.0 mm membrane could indicate that the hydrogen permeation flux through these specimens is controlled by different rate determining steps. The permeation through the thicker membrane should be controlled by bulk diffusion and the thinner membrane could be affected more by the surface exchange kinetics.

Table 7-1. Activation energies (in eV) for hydrogen permeation flux of membranes of different thickness and different feed-side hydrogen partial pressures

	0.1 atm	0.5 atm	0.9 atm
0.75 mm	0.90±0.03	0.90±0.04	0.95±0.03
1.0 mm	0.83±0.02	0.87±0.02	0.84±0.01
2.0 mm	0.77±0.01	0.83±0.02	0.80±0.01

7.3.2 Hydrogen Partial Pressure Dependence

Figure 7-4 shows the hydrogen permeation flux at 750°, 800°, and 850°C as a function of feed-side hydrogen partial pressure for varying thicknesses. The hydrogen flux for the 1.0 mm and 2.0 mm membranes varies linearly with the logarithm of hydrogen partial pressure at all temperatures. The constant slope indicates that the ambipolar conductivity does not change under feed-side hydrogen partial pressure. The mean values of the ambipolar conductivity for the $BaCe_{0.85}Eu_{0.15}O_{3-\delta}$ membranes, evaluated from the slopes of the curves in figure 7-4, are given in table 7-2. The values for the 0.75 mm membrane are not given since the flux values are not linear with partial pressure.

Table 7-2. Ambipolar conductivity (in S/cm) estimated from figure 7-4

	750°C	800°C	850°C
1.0 mm	1.4e-3	1.1e-3	7.2e-3
2.0 mm	2.6e-3	1.8e-3	1.3e-3

7.3.3 Thickness Dependence

As shown in figure 7-5, the hydrogen flux varies linearly with inverse thickness at 750°, 800°, and 850°C for all feed-side hydrogen partial pressures. This relationship would indicate that Wagner's theory applies and bulk diffusion controls permeation in the membrane thickness range tested (0.75-2.00 mm). Analysis of the flux according to equation 7-3 demonstrates a different result. The log-log plot of hydrogen versus membrane thickness for 750°, 800°, and 850°C with a feed-side partial pressure of 0.9 atm is shown in figure 7-6. The values of γ determined from the negative slopes in figure 7-5 were 0.32, 0.43, and 0.51 at 750°, 800°, and 850°C, respectively. These values for γ indicate that in the range of thicknesses and temperatures investigated the performance of the membrane is under mixed control of bulk diffusion and surface kinetics.

7.3.4 Membrane Surface Modification

Surface modification using a porous platinum catalyst layer on both sides of a 1.0 mm $BaCe_{0.85}Eu_{0.15}O_{3-\delta}$ membrane resulted in enhanced hydrogen flux. The temperature dependence of hydrogen flux at all feed-side hydrogen partial pressures for a modified and membrane is shown in figure 7-7. A two way analysis of variance found that there is a statistically significant difference between the hydrogen fluxes of the modified and unmodified membranes (compared using the Tukey test) between 650°C and 850°C under all feed-side hydrogen partial pressures. For all three hydrogen conditions, the activation energy for hydrogen flux decreases for the modified membrane compared to the unmodified one. The increase in hydrogen flux and decrease in activation energy due to the porous platinum layer confirm that the hydrogen surface exchange kinetics definitely affect the flux of hydrogen through a 1 mm thick $BaCe_{0.85}Eu_{0.15}O_{3-\delta}$ membrane. Concurrently decreasing the membrane thickness and applying catalytic surface layers should result in increased hydrogen flux.

7.3.5 Effect of A:B Stoichiometry

The effect of varying the A:B stoichiometry of $BaCe_{0.85}Eu_{0.15}O_{3-\delta}$ on the hydrogen permeation flux is shown in figure 7-8 for different feed-side partial pressures. A two way analysis of variance showed that over the temperature range investigated the difference in hydrogen permeation flux of the membranes was not statistically significant under feed-side hydrogen partial pressures of 0.5 and 0.9 atm. The membrane with A:B=1.01 does demonstrate a higher activation energy at all three feed-side pressures. This higher activation energy could result from excess BaO existing as an amorphous grain boundary phase, which is not detected by x-ray diffraction, as proposed by Kreuer et al.[69] The insignificant difference in hydrogen permeation flux of the stoichiometric and the barium deficient membranes indicates that further membrane research concerned with chemical stability can progress with the barium deficient compounds without a loss in flux.

7.3.6 Effect of Sm and Yb Dopants

The barium cerate membrane doped with samarium, $BaCe_{0.85}Sm_{0.15}O_{3-\delta}$, tended to have a higher hydrogen permeation flux than both the Eu-doped and Yb-doped membranes over the temperature range and feed-side hydrogen partial pressure range studied (Figure 7-9). Over the same ranges, the Eu-doped membrane tended to have a higher flux than the Yb-doped membrane. The electronic conduction of these materials depends on the electron transfers from a dopant ion in a low-oxidation state, M^{2+} (M_{Ce}'' using Kroger Vink notation), to a neighboring ion in a high oxidation state, M^{3+} (M_{Ce}') (Equation 7-7).

$$M_{Ce}'' \rightarrow M_{Ce}' + e' \tag{7-7}$$

All three dopants exhibit multivalent character (+3/+2) with third ionization potentials (Equation 7-8) of 23.4, 24.9, and 25.03 eV for Sm, Eu, and Yb, respectively.[114]

$$M^{2+} \rightarrow M^{3+} + e' \text{ (third ionization potential)} \tag{7-8}$$

Song et al.[66] found that for $SrCe_{0.95}M_{0.05}O_{3-\delta}$ (M= Eu, Sm), the higher hydrogen permeation fluxes resulted from doping with Eu rather than Sm. Since the Eu^{2+} to Eu^{3+} transition is more thermodynamically stable than Sm^{2+} to Sm^{3+}, there would be a greater concentration of Eu^{2+} than Sm^{2+} resulting in a greater n-type electronic conduction in $SrCe_{0.95}Eu_{0.05}O_{3-\delta}$ thus a higher hydrogen permeation flux. The opposite effect seems to occur with the $BaCe_{0.85}M_{0.15}O_{3-\delta}$ (M= Sm, Eu, Yb) system where doping with the less thermodynamically stable multivalent dopant actually results in an increase in electronic conduction which leads to an increase in hydrogen permeation flux. The membranes analyzed by Song et al.[66] were not surface-modified so it is possible that they were surface exchange limited while the membranes used in our study were surface-modified so they could be bulk diffusion limited. Further work is necessary to understand this phenomenon.

7.4 Conclusions

The hydrogen permeation flux of $BaCe_{0.85}Eu_{0.15}O_{3-\delta}$ membranes was analyzed as a function of temperature, membrane thickness, and feed-side hydrogen partial pressure to understand the effect of bulk diffusion and surface exchange kinetics. In the temperature range of 650°C to 850°C, the difference in activation energy for hydrogen flux between a 0.75 mm (~0.9eV) and 2.00 mm (~0.8 eV) membrane indicates a possible change in the rate determining step from bulk hydrogen diffusion for the 2.00 mm membrane to surface hydrogen exchange for the 0.75 mm membrane. Further analysis of the membranes as a function of thickness indicated that in the range of 0.75 mm to 2.00 mm, the $BaCe_{0.85}Eu_{0.15}O_{3-\delta}$ membranes are actually under mixed control of bulk diffusion and surface exchange kinetics. The effect of surface exchange kinetics increases with decreasing temperature. Surface modification of a 1.00 mm membrane with a porous platinum layer resulted in a statistically significant increase in hydrogen permeation flux compared to an unmodified membrane. The increase in flux with the modified surfaces indicates that surface exchange kinetics drastically effect hydrogen permeation and must be considered when trying to decrease membrane thickness for improved hydrogen permeation. Varying the A:B site stoichiometry of the $BaCe_{0.85}Eu_{0.15}O_{3-\delta}$ membranes resulted in minimal changes in hydrogen permeation flux which were determined to be statistically insignificant. Surface modified barium cerate membranes doped with samarium and with ytterbium were also studied. The samarium-doped membrane exhibited a higher hydrogen permeation flux than the europium-doped membrane over the temperature range and feed-side hydrogen partial pressure range studied. The ytterbium-doped membrane had a lower hydrogen permeation flux than both of the other membranes. Further research of $BaCe_{0.85}M_{0.15}O_{3-\delta}$ (M= Sm, Eu) as a hydrogen membrane material must focus on decreasing the thickness of the membrane, determining the optimal method of surface modification (both material and technique), and possibly working with barium deficient compounds when considering chemical stability.

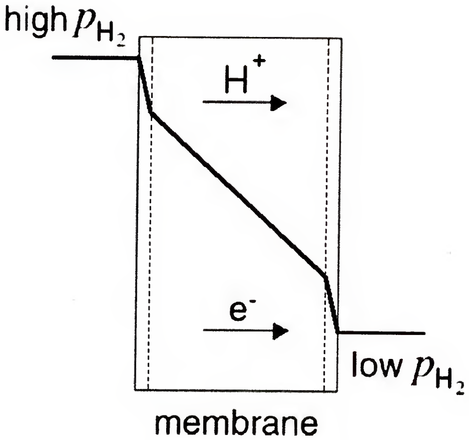

Figure 7-1. Schematic of a hydrogen membrane under a hydrogen chemical potential gradient assuming linear kinetics. The surface layers are exaggerated to show the hydrogen potential gradient being partially consumed by surface exchange kinetics.

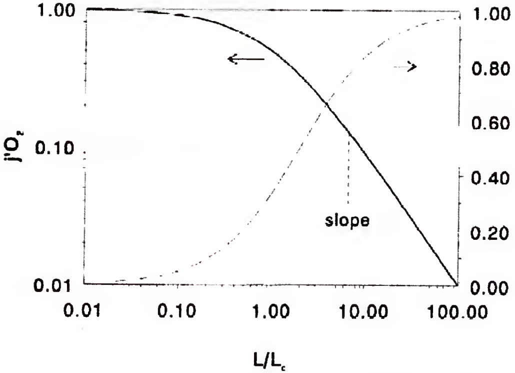

Figure 7-2. Thickness dependence on oxygen flux and γ indicating the transition from a bulk limited regime ($L >> L_c$) to a surface exchange limited regime ($L << L_c$) [from ref 67]

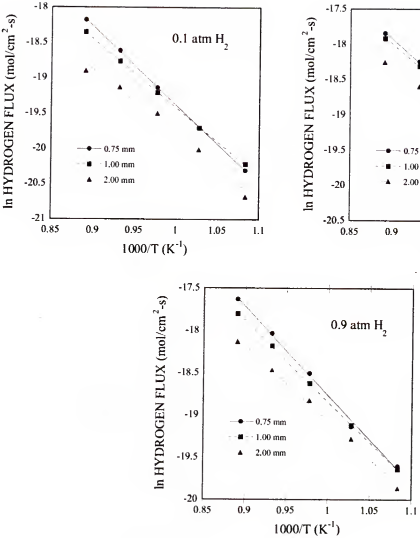

Figure 7-3. Temperature dependence of hydrogen permeation flux of $BaCe_{0.85}Eu_{0.15}O_{3-\delta}$ at different feed-side partial pressures and thicknesses

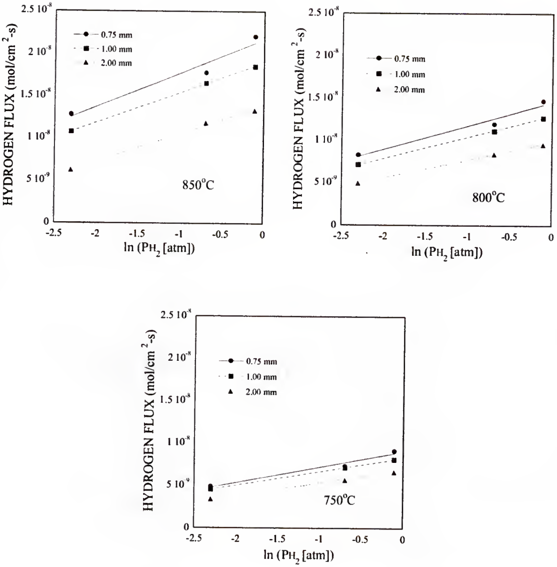

Figure 7-4. Feed-side hydrogen partial pressure dependence of hydrogen permeation flux of $BaCe_{0.85}Eu_{0.15}O_{3-\delta}$ at 750°, 800°, and 850°C for membranes of different thicknesses

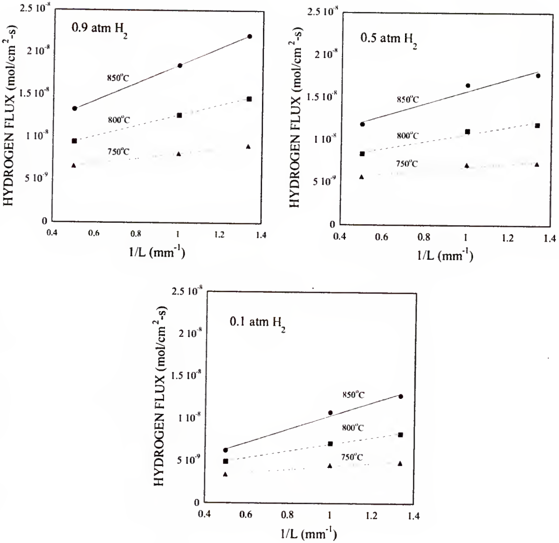

Figure 7-5. Hydrogen permeation flux as a function of inverse membrane thickness

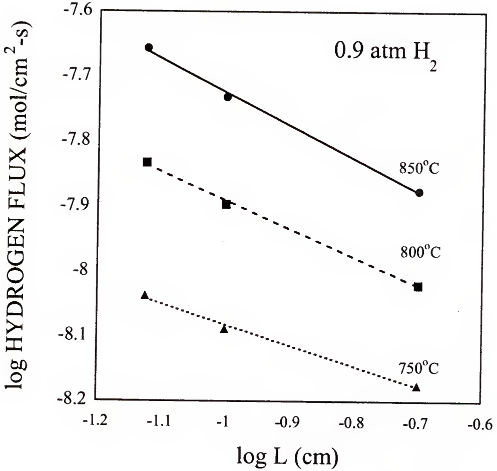

Figure 7-6. Log-Log plot of hydrogen permeation flux as a function of thickness

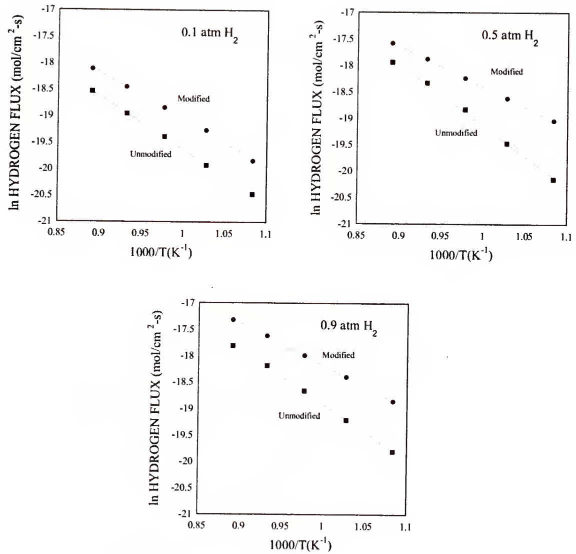

Figure 7-7. Temperature dependence of hydrogen permeation flux for Pt surface modified and unmodified $BaCe_{0.85}Eu_{0.15}O_{3-\delta}$ membranes at different feed-side hydrogen partial pressures

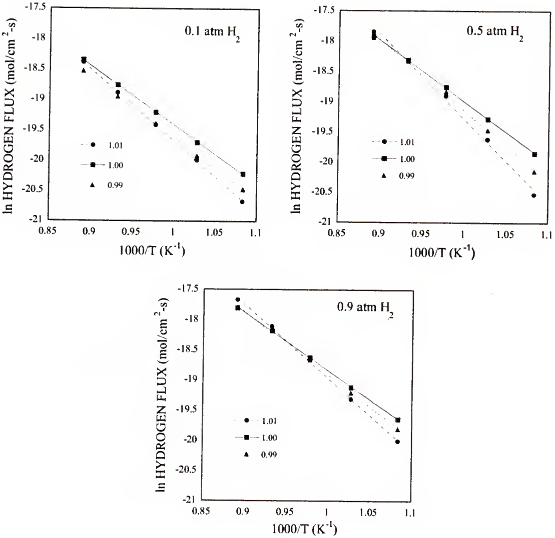

Figure 7-8. Temperature dependence of hydrogen permeation flux at different feed-side hydrogen partial pressures for varying A:B site stoichiometries (0.99, 1.00, and 1.01)

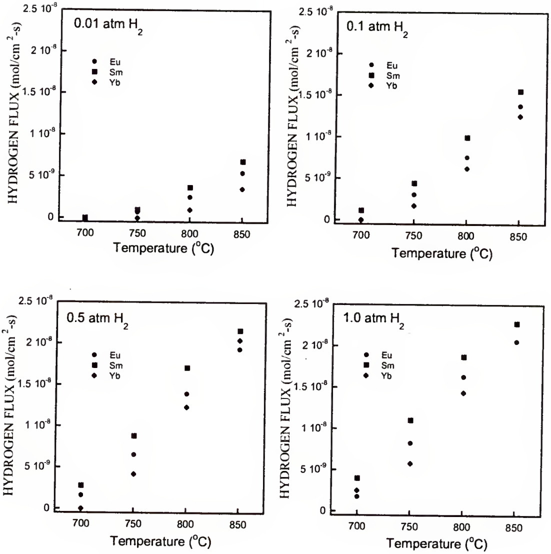

Figure 7-9. Temperature dependence of hydrogen permeation flux of $BaCe_{0.85}M_{0.15}O_{3-\delta}$ (M = Eu, Sm, Yb)under different feed-side hydrogen partial pressures (0.01, 0.1, 0.5, 1.0 atm)

CHAPTER 8
CONCLUSIONS

The electrical conductivity and hydrogen permeation flux of single phase europium-doped barium cerate were studied to determine its potential applicability as a hydrogen separation membrane material. Predominantly single phase barium cerate ($BaCeO_3$) powders were prepare via solid state reaction of barium carbonate, cerium (IV) oxide, and europium (III) oxide or gadolinium oxide. The europium (Eu) or gadolinium (Gd) was doped onto the Ce-site (B-site in the ABO_3 perovskite) of the $BaCeO_3$. For the powders which were calcined at 1350°C, a sintering temperature of 1650°C was necessary to achieve the densest microstructure

The electrical conductivity of both 15 mol% Gd-doped $BaCeO_3$ and 15 mol% Eu-doped $BaCeO_3$ samples was measured between 450° and 750°C in wet forming gas (4% hydrogen/96% nitrogen) using a.c. impedance spectroscopy. The Eu-doped $BaCeO_3$ exhibited a higher conductivity than the Gd-doped $BaCeO_3$ which is known to have one of the highest conductivities in hydrogen-containing atmospheres at the temperatures studied. The electrical conductivities of different Eu dopant levels (5-25 mol%) were also measured between 450° and 800°C in dry forming gas, dry air, and wet nitrogen. The 15 mol% Eu-doped samples exhibited the highest conductivity in all three conditions. This composition was selected for further study.

The conductivity for 15 mol% Eu-doped $BaCeO_3$ was determined in dry forming gas, dry air, and wet nitrogen was the total conductivity which is the sum of the conductivities of all potential charge carriers (ionic and electronic). The mixed ionic-electronic conductivity of 15 mol% Eu-doped $BaCeO_3$ was examined by measuring conductivity as a function of oxygen partial pressure and hydrogen partial pressure. The onset temperature for n-type electronic conductivity was ~600°C for 15 mol% Eu-doped $BaCeO_3$. The conductivity of 15 mol% Eu-doped $BaCeO_3$ demonstrated a gradual increase with increasing hydrogen partial pressure.

A quartz and alumina apparatus was constructed to examine the hydrogen permeation properties of 15 mol% Eu-doped $BaCeO_3$. Different commercial glasses were investigated to seal the barium cerate membrane to an alumina tube between 600° and 900°C. Borosilicate and aluminosilicate glasses exhibited poor wetting properties with the alumina tube and could not be used. Two other glasses, Elan 63 and SEM-COM SCC-5, sealed the membranes at 850°C and 725°C respectively, but they also reacted with the surfaces of the membranes. The successful sealing material was a composite of a glass with the same composition as Argonne National Laboratory Mat43[102] and barium cerate powder. The seal was formed at ~875°C allowing for testing from 850° to 650°C. Testing with a dense alumina disc demonstrated no hydrogen diffusion through the glass so all hydrogen measured during permeation experiments results from hydrogen permeation through the membrane.

The effect of temperature, feed-side hydrogen partial pressure, and membrane thickness on hydrogen permeation of 15 mol% Eu-doped $BaCeO_3$ was investigated. In the temperature range of 650°C to 850°C, the difference in activation energy for hydrogen flux between a 0.75 mm and 2.00 mm membrane indicates a possible change in the rate determining step from bulk hydrogen diffusion for the 2.00 mm membrane to surface hydrogen exchange for the 0.75 mm membrane. Analysis of membranes as a function of thickness indicates that the $BaCe_{0.85}Eu_{0.15}O_{3-\delta}$ membranes are actually under mixed control of bulk diffusion and surface exchange kinetics. The effect of surface exchange kinetics increases with decreasing temperature. Membrane surface modification with a porous platinum layer resulted in a statistically significant increase in hydrogen permeation flux compared to a unmodified membrane. The increase in flux with the modified surfaces indicates that surface exchange kinetics drastically effect hydrogen permeation and must be considered when trying to decrease membrane thickness for improved hydrogen permeation. Varying the A:B (Ba:Ce) site stoichiometry of the $BaCe_{0.85}Eu_{0.15}O_{3-\delta}$ membranes resulted in a statistically insignificant difference in hydrogen permeation flux over the temperature range studied for 0.5 and 0.9 atm feed-side hydrogen partial pressures. A surface-modified barium cerate doped with 15 mol% samarium had a higher hydrogen permeation flux than a europium-doped sample over the temperature range and the feed-side hydrogen partial pressure range studied.

APPENDIX A
REPRESENTATIVE IMPEDANCE PLOTS

The following figures are provided to give a representation of some of the impedance plots used to determine the conductivities of various materials studied. Figures A-1a and A-1b are impedance spectra used to determine the conductivities of barium cerate samples in forming gas with different europium dopant levels (10, 20, and 25 mol%) at 600°C and 800°C, respectively. Figures A-2a and A-2b are impedance spectra used to determine the conductivity of 15 mol% Eu-doped barium cerate as a function of hydrogen partial pressure at 600°C and 800°C, respectively.

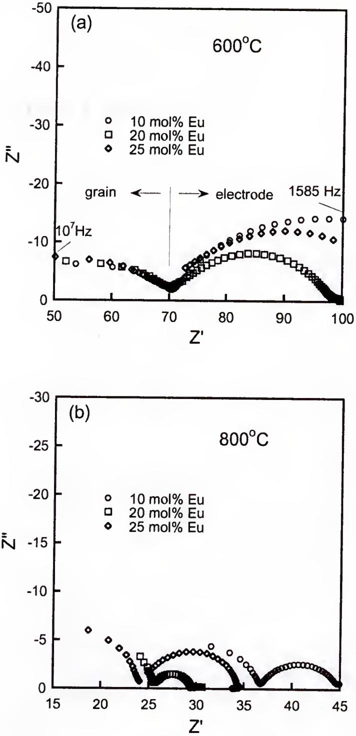

Figure A-1. Representative impedance spectra used to determine the conductivities of europium-doped barium cerates at different dopant levels (10, 20, and 25 mol%) in dry forming gas. (a) Spectra collected at 600°C and (b) Spectra collected at 800°C

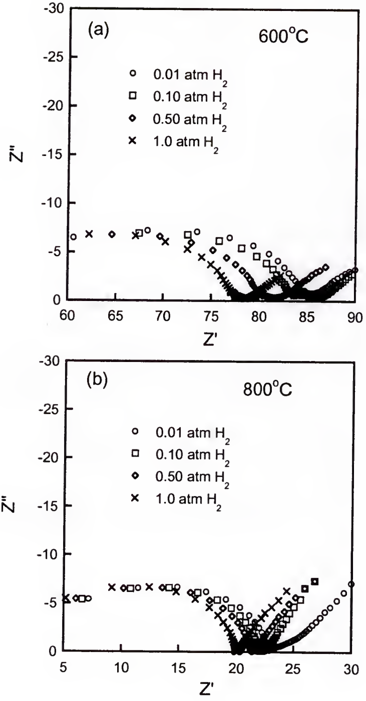

Figure A-2. Representative impedance spectra used to determine the conductivities of 15 mol% Eu-doped barium cerate as a function of hydrogen partial pressure (0.01, 0.1, 0.5, 1.0 atm H_2). (a) Spectra collected at 600°C and (b) Spectra collected at 800°C

LIST OF REFERENCES

1. U.S. and World Population Clocks. U.S. Census Bureau. http://www.census.gov/main/www/popclock.html (December 2004).

2. International Energy Outlook 2004. Energy Information Administration. http://www.eia.doe.gov/oiaf/ieo/world.html (December 2004).

3. Department of Economic and Social Affairs Population Division. United Nations. http://www.un.org/esa/population/unpop.htm (December 2004).

4. Romm, J. J., *The Hype About Hydrogen*. Island Press: Washington D.C., 2004; p 238.

5. Dyer, P. N.; Richards, R. E.; Russek, S. L.; Taylor, D. M. Ion transport membrane technology for oxygen separation and syngas production. *Solid State Ionics* **2000,** 134, 21.

6. *DOE Hydrogen Program Strategic Plan*; DOE/GO-10098-532; Department of Energy: Washington, D.C., Jan 1998.

7. Meindersma, G. W.; Kuczynski, M. Implementing membrane technology in the process industry: problems and opportunities. *J. Membr. Sci.* **1996,** 113, 285.

8. Buxbaum, R. E.; Kinney, A. B. Hydrogen transport through tubular membranes of palladium-coated tantalum and niobium. *Ind. Eng. Chem. Res.* **1996,** 35, (2), 530.

9. Li, A.; Liang, W.; Hughes, R. Characterisation and permeation of palladium/stainless steel composite membranes. *J. Membr. Sci.* **1998,** 149, (2), 259.

10. Julbe, A.; Farrusseng, D.; Guizard, C. Porous ceramic membranes for catalytic reactors - overview and new ideas. *J. Membr. Sci.* **2001,** 181, 3.

11. Paglieri, S. N.; Way, J. D. Innovations in palladium membrane research. *Sep. Purif. Methods* **2002,** 31, (1), 1.

12. Uemiya, S. State-of-the-art of supported metal membranes for gas separation. *Sep. Purif. Methods* **1999,** 28, (1), 51.

13. Julbe, A.; Ramsay, J. D. F. Methods for the characterisation of porous structure in membrane materials. In *Fundamentals of Inorganic Membrane Science and Technology*, Burggraaf, A. J., Cot, L., Eds.; Elsevier Science B.V.: Amsterdam, 1996.

14. Jansen, K. C.; Coker, E. N. Zeolitic membranes. *Curr. Opin. Mater. Sci.* **1996,** 1, 65.

15. Lee, D.; Oyama, S. T. Gas permeation characteristics of a hydrogen selective supported silica membrane. *J. Membr. Sci.* **2002,** 210, 291.

16. Casanave, D.; Giroir-Fendler, A.; Sanchez, J.; Loutaty, R.; Dalmon, J.-A. Control of transport properties with a microporous membrane reactor to enhance yields in dehydrogenation reactions. *Catal. Today* **1995,** 25, 309.

17. Coronas, J.; Santamaria, J. Catalytic reactors based on porous ceramic membranes. *Catal. Today* **1999,** 51, 377.

18. Kajiwara, M.; Uemiya, S.; Kojima, T.; Kikuchi, E. Rhodium- and iridium-dispersed porous alumina membranes and their hydrogen permeation properties. *Catal. Today* **2000,** 56, 83.

19. Yildirim, Y.; Gobina, E.; Hughes, R. An experimental evaluation of high-temperature composite membrane systems for propane dehydrogenation. *J. Membr. Sci.* **1997,** 135, 107.

20. So, J. H.; Yang, S. M.; Park, S. B. Preparation of silica-alumina composite membranes for hydrogen separation by multi-step pore modifications. *J. Membr. Sci.* **1998,** 147, 147.

21. Iwahara, H. Hydrogen pumps using proton-conducting ceramics and their applications. *Solid State Ionics* **1999,** 125, 271.

22. Matsumoto, H.; Asakura, F.; Takeuchi, K.; Iwahara, H. Transient phenomena of an electrochemical hydrogen pump using a $SrCeO_3$-based proton conductor. *Solid State Ionics* **2000,** 129, 209.

23. Iwahara, H.; Matsumoto, H.; Takeuchi, K. Electrochemical dehumidification using proton conducting ceramics. *Solid State Ionics* **2000,** 136-137, 133.

24. Kim, J.; Lin, Y. S. Synthesis and oxygen permeation properties of ceramic-metal dual-phase membranes. *J. Membr. Sci.* **2000,** 167, 123.

25. Chen, C. S.; Kruidhof, H.; Bouwmeester, H. J. M.; Verweij, H.; Burggraaf, A. J. Oxygen permeation through oxygen ion oxide-noble metal dual phase composites. *Solid State Ionics* **1996,** 86-88, 569.

26. Iwahara, H.; Esaka, T.; Uchida, H.; Maeda, N. Proton Conduction in Sintered Oxides and Its Application to Steam Electrolysis for Hydrogen-Production. *Solid State Ionics* **1981,** 3-4, 359.

27. Iwahara, H.; Uchida, H.; Ono, K.; Ogaki, K. Proton conduction in sintered oxides based on $BaCeO_3$. *J. Electrochem. Soc.* **1988,** 135, (2), 529.

28. Scherban, T.; Nowick, A. S. Bulk protonic conduction in Yb-doped $SrCeO_3$. *Solid State Ionics* **1989,** 35, 189.

29. Bonanos, N. Transport properties and conduction mechanism in high-temperature protonic conductors. *Solid State Ionics* **1992,** 53-56, 967.

30. Hibino, T.; Mizutani, K.; Yajima, T.; Iwahara, H. Evaluation of proton conductivity in $SrCeO_3$, $BaCeO_3$, $CaZrO_3$, and $SrZrO_3$ by temperature programmed desorption method. *Solid State Ionics* **1992,** 57, 303.

31. Stevenson, D. A.; Jiang, N.; Buchanan, R. M.; Henn, F. E. G. Characterization of Gd, Yb, and Nd doped barium cerates as proton conductors. *Solid State Ionics* **1993,** 62, 279.

32. Iwahara, H.; Yajima, T.; Hibino, T.; Ushida, H. Performance of solid oxide fuel cell using proton and oxide ion mixed conductors $BaCe_{1-x}Sm_xO_{3-\alpha}$. *J. Electrochem. Soc.* **1993,** 140, (6), 1687.

33. Iwahara, H. Technological challenges in the application of proton conducting ceramics. *Solid State Ionics* **1995,** 77, 289.

34. Bonanos, N.; Ellis, B.; Mahmood, M. N. Oxide ion conduction in ytterbium-doped strontium cerate. *Solid State Ionics* **1988,** 28-30, 579.

35. Kosacki, I.; Becht, J. G. M.; van Landschoot, R.; Schoonman, J. Electrical properties of $SrCe_{0.95}Yb_{0.05}O_3$ in hydrogen containing atmospheres. *Solid State Ionics* **1993,** 59, 287.

36. Zheng, M.; Zhu, B. Proton conductivity in Yb-doped strontium cerates. *Solid State Ionics* **1995,** 80, 59.

37. de Vries, K. J. Electrical and mechanical properties of proton conducting $SrCe_{0.95}Yb_{0.05}O_{3-\alpha}$. *Solid State Ionics* **1997,** 100, 193.

38. Iwahara, H.; Yajima, T.; Ushida, H. Effect of ionic radii of dopants on mixed ionic conduction (H^++O^{2-}) in $BaCeO_3$-based electrolytes. *Solid State Ionics* **1994,** 70/71, 267.

39. Bonanos, N. Oxide-based protonic conductors: point defects and transport properties. *Solid State Ionics* **2001,** 145, (1-4), 265.

40. Kreuer, K.-D. Proton conductivity: materials and applications. *Chem. Mater.* **1996,** 8, 610.

41. Norby, T. Proton conduction in oxides. *Solid State Ionics* **1990,** 40-41, 857.

42. Kreuer, K. D. Proton-conducting oxides. *Ann. Rev. Mater. Res.* **2003,** 33, 333.

43. Kreuer, K.-D.; Dippel, T.; Hainovsky, N. G.; Maier, J. Proton conductivity: compounds and their structural and chemical peculiarities. *Ber. Bunsen-Ges. Phys. Chem.* **1992,** 96, (11), 1736.

44. Scherban, T.; Villeneuve, R.; Abello, L.; Lucazeau, G. Raman scattering study of acceptor-doped $BaCeO_3$. *Solid State Ionics* **1993,** 61, 93.

45. Liang, K. C.; Du, Y.; Nowick, A. S. Fast high-temperature proton transport in nonstoichiometric mixed perovskites. *Solid State Ionics* **1994,** 69, 117.

46. Kreuer, K.-D.; Fuchs, A.; Maier, J. H/D isotope effect of proton conductivity and proton conduction mechanism in oxides. *Solid State Ionics* **1995,** 77, 157.

47. Matushita, E.; Tanase, A. Theoretical approach for protonic conduction in perovskite-oxide ceramics. *Solid State Ionics* **1997,** 97, 45.

48. Munch, W.; Seifert, G.; Kreuer, K. D.; Maier, J. A quantum molecular dynamics study of proton conduction phenomena in $BaCeO_3$. *Solid State Ionics* **1996,** 86-88, 647.

49. Munch, W.; Seifert, G.; Kreuer, K.-D.; Maier, J. A quantum molecular dynamics study of the cubic phase of $BaTiO_3$ and $BaZrO_3$. *Solid State Ionics* **1997,** 97, 39.

50. Islam, M. S.; Davies, R. A.; Gale, J. D. Hop, skip or jump? Proton transport in the $CaZrO_3$ perovskite oxide. *Chem. Comm.* **2001,** 2001, (7), 661.

51. Kreuer, K. D. On the development of proton conducting materials for technological applications. *Solid State Ionics* **1997,** 97, 1.

52. Kreuer, K. D. Aspects of the formation and mobility of protonic charge carriers and the stability of perovskite-type oxides. *Solid State Ionics* **1999,** 125, 285.

53. Kreuer, K.-D. On the complexity of proton conduction phenomena. *Solid State Ionics* **2000,** 136-137, 149.

54. Preda, M.; Dinescu, R. Thermal equilibria in the binary systems $MgO-CeO_2$, $CaO-CeO_2$, $SrO-CeO_2$, $BaO-CeO_2$. *Rev. Roum. Chim.* **1976,** 24, (7), 1023.

55. Longo, V.; Ricciardiello, F.; Minichelli, D. X-ray characterization of $SrCeO_3$ and $BaCeO_3$. *J. Mater. Sci. Lett.* **1981,** 16, 3503.

56. Smith, A. J.; Welch, A. J. E. Some mixed metal oxides of perovskite structure. *Acta Crystallogr.* **1960,** 13, 653.

57. Jacobson, A. J.; Tofield, B. C.; Fender, B. E. F. The structures of $BaCeO_3$, $BaPrO_3$, and $BaTbO_3$ by neutron diffraction: lattice parameter relations and ionic radii in *O*-perovskites. *Acta Crystallogr.* **1972,** B28, 956.

58. Knight, K. S. Structural phase transitions in $BaCeO_3$. *Solid State Ionics* **1994,** 74, 109.

59. Knight, K. S.; Bonanos, N. The crystal structures of some doped and undoped alkaline earth cerate perovskites. *Mater. Res. Bull.* **1995,** 30, (3), 347.

60. Knight, K. S. Structural phase transitions, oxygen vacancy ordering and protonation in doped $BaCeO_3$: results from time-of-flight neutron powder diffraction investigations. *Solid State Ionics* **2001,** 145, 275.

61. Hamakawa, S.; Hibino, T.; Iwahara, H. Electrochemical hydrogen permeation in a proton-hole mixed conductor and its application to a membrane reactor. *J. Electrochem. Soc.* **1994,** 141, (7), 1720.

62. Guan, J.; Dorris, S. E.; Balachandran, U. Transport properties of $SrCe_{0.95}Y_{0.05}O_{3-\delta}$ and its application for hydrogen separation. *Solid State Ionics* **1998,** 110, 303.

63. Qi, X.; Lin, Y. S. Electrical conduction and hydrogen permeation through mixed proton-electron conducting strontium cerate membranes. *Solid State Ionics* **2000,** 130, 149.

64. Li, L.; Iglesia, E. Synthesis and characterization of proton-conducting oxides as hydrogen transport membranes. *Stud. Surf. Sci. Catal.* **2001,** 136, 357.

65. Hamakawa, S.; Li, L.; Li, A.; Iglesia, E. Synthesis and hydrogen permeation properties of membranes based on dense $SrCe_{0.95}Yb_{0.05}O_{3-\alpha}$ thin films. *Solid State Ionics* **2002,** 48, 71.

66. Song, S. J.; Wachsman, E. D.; Rhodes, J.; Dorris, S. E.; Balachandran, U. Hydrogen permeability of $SrCe_{1-x}M_xO_{3-\delta}$ (x=0.05, M=Eu, Sm). *Solid State Ionics* **2004,** 167, (1-2), 99.

67. Bouwmeester, H. J. M.; Burggraaf, A. J. Chapter 14: Dense ceramic membranes for oxygen separation. In *The CRC Handbook of Solid State Electrochemistry*, Gellings, P. J., Bouwmeester, H. J. M., Eds.; CRC Press: Boca Raton, FL, 1997.

68. Iwahara, H. Proton conducting ceramics and their applications. *Solid State Ionics* **1996,** 86-88, 9.

69. Kreuer, K. D.; Schonherr, E.; Maier, J. Phase separation and grain boundary proton conductivity in $BaCeO_3$ based ceramics. In *14th Risø International Society Materials Science*, 1993; pp 297-304.

70. Advanced Instrumentation for Solid State Applications. Solartron-Analytical. http://www.solartronanalytical.com/technicalpages/techsolidstate.html (November 2004).

71. Jiang, S. P.; Love, J. G.; Badwal, S. P. S. Electrochemical techniques in studies of solid ionic conductors. *Key Eng. Mat.* **1997,** 125-126, 81.

72. *Fundamentals of vacuum technology*. Leybold Vacuum: Cologne, 1998; Vol. 09/98, p 188.

73. O'Hanlon, J. F., *A user's guide to vacuum technology*. John Wiley & Sons: New York, 1989; p 481.

74. Cullity, B. D.; Stock, S. R., *Elements of x-ray diffraction*. Prentice Hall: Upper Saddle River, NJ, 2001; p 664.

75. Tissue, B. M. Quadrupole Mass Spectrometry. http://www.chem.vt.edu/chem-ed/ms/quadrupo.html (May 2004).

76. Iwahara, H.; Hibino, T.; Yamada, M. SOFC using Dy-doped $BaCeO_3$ ceramics as a solid electrolyte. In *Third International Symposium on Solid Oxide Fuel Cells at the 183rd Meeting of The Electrochemical Society*, Honolulu, Hawaii, Singhal, S. C., Iwahara, H., Eds.; The Electrochemical Society: 1993; pp 137-145.

77. Park, E. T.; Goretta, K. C.; de Arellano-Lopez, A. R.; Guan, J.; Balachandran, U.; Dorris, S. E.; Routbort, J. L. High-temperature deformation of $BaCe_{1-x}Y_xO_{3-y}$ (0.05<=x<=0.2). *Solid State Ionics* **1999,** 117, 323.

78. Bohn, H. G.; Schober, T. Electrical conductivity of the high-temperature proton conductor $BaZr_{0.9}Y_{0.1}O_{2.95}$. *J. Am. Ceram. Soc.* **2000,** 83, (4), 768.

79. Slade, R. C. T.; Singh, N. Systematic examination of hydrogen ion conduction in rare-earth doped barium cerate ceramics. *Solid State Ionics* **1991,** 46, 111.

80. Slade, R. C. T.; Singh, N. The perovskite-type proton-conducting solid electrolyte $BaCe_{0.90}Y_{0.10}O_{3-\alpha}$. *Solid State Ionics* **1993,** 61, 111.

81. Browning, D.; Weston, J. B.; Lakeman, J. B.; Jones, P.; Cherry, M.; Irvine, J. T. S.; Corcoran, D. J. D. Proton conducting ceramics for use in intermediate temperature proton conducting fuel cells. *J. New Mat. Electrochem. Systems* **2002,** 5, 25.

82. Reichel, U.; Arons, R. R.; Schilling, W. Investigation of n-type electronic defects in the protonic conductor $SrCe_{1-x}Y_xO_{3-\delta}$. *Solid State Ionics* **1996,** 86-88, 639.

83. Kosacki, I.; Tuller, H. L. Mixed conductivity in $SrCe_{0.95}Yb_{0.05}O_3$ protonic conductors. *Solid State Ionics* **1995,** 80, 223.

84. Phillips, R. J.; Bonanos, N.; Poulsen, F. W.; Ahlgren, E. O. Structural and electrical characterisation of $SrCe_{1-x}Y_xO_\varepsilon$. *Solid State Ionics* **1999,** 125, 389.

85. Bonanos, N. Transport study of the solid electrolyte $BaCe_{0.9}Gd_{0.1}O_{2.95}$ at high temperatures. *J. Phys. Chem. Solids* **1993,** 54, (7), 867.

86. Tuller, H. L. Mixed conduction in nonstoichiometric oxides. In *Nonstoichimetric Oxides*, Sorensen, O. T., Ed. Academic Press: New York, 1981.

87. Tuller, H. L.; Nowick, A. S. Small polaron electron transport in reduced CeO_2 single crystals. *J. Phys. Chem. Solids* **1977,** 38, 859.

88. Paiva, O. C.; Barbosa, M. A. Production, bond strength and electrochemical behavior of commercially pure Ti/Al_2O_3 brazed joints. *J. Mater. Sci.* **1997,** 32, 653.

89. Eiter, J.; Kock, W.; Huber, T. Hard solder. U.S. Patent 5,830,292, Nov 1998.

90. Velterop, F. M. Method of connecting ceramic material to another material. Netherlands Patent 5,139,191, Aug 1992.

91. Teraoka, Y.; Zhang, H.-M.; Furukawa, S.; Yamazoe, N. Oxygen permeation through perovskite-type oxides. *Chem. Lett.* **1985**, 1743.

92. Teraoka, Y.; Honbe, Y.; Ishii, J.; Furukawa, H.; Moriguchi, I. Catalytic effects in oxygen permeation through mixed-conductive LSCF perovskite membranes. *Solid State Ionics* **2002,** 152-153, 681.

93. Carter, S.; Selcuk, A.; Chater, R. J.; Kajda, J.; Kilner, J. A.; Steele, B. C. H. Oxygen transport in selected non-stoichiometric perovskite-structure oxides. *Solid State Ionics* **1992,** 53-56, 597.

94. Zeng, Y.; Lin, Y. S.; Swartz, S. L. Perovskite-type ceramic membrane: synthesis, oxygen permeation and membrane reactor performance for oxidative coupling of methane. *J. Membr. Sci.* **1998,** 150, 87.

95. Lane, J. A.; Benson, S. J.; Waller, D.; Kilner, J. A. Oxygen transport in $La_{0.6}Sr_{0.4}Co_{0.2}Fe_{0.8}O_{3-\delta}$. *Solid State Ionics* **1999,** 121, 201.

96. Qiu, L.; Lee, T. H.; Liu, M.; Yang, Y. L.; Jacobson, A. J. Oxygen permeation studies of $SrCo_{0.8}Fe_{0.2}O_{3-\delta}$. *Solid State Ionics* **1995,** 76, 321.

97. Balachandran, U.; Ma, B.; Maiya, P. S.; Mieville, R. L.; Dusek, J. T.; Picciolo, J. J.; Guan, J.; Dorris, S. E.; Liu, M. Development of mixed-conducting oxides for gas separation. *Solid State Ionics* **1998,** 108, 363.

98. Guan, J.; Dorris, S. E.; Balachandran, U.; Liu, M. Transport properties of $BaCe_{0.95}Y_{0.05}O_{3-\alpha}$ mixed conductors for hydrogen separation. *Solid State Ionics* **1997,** 100, 45.

99. Maiya, P. S.; Picciolo, J. J.; Emerson, J. E.; Dusek, J. T.; Balachandran, U. High temperature seal for joining ceramics and metal alloys. U.S. Patent 5,725,218, Mar 1998.

100. Schutz, J. B.; Barton, T. F. Glass-ceramic seals for ceramic membrane chemical reactor. U.S. Patent 6,402,156, Jun 2002.

101. Qi, X.; Akin, F. T.; Lin, Y. S. Ceramic-glass composite high temperature seals for dense ionic-conducting ceramic membranes. *J. Membr. Sci.* **2001,** 193, 185.

102. Ley, K. L.; Krumpelt, M.; Kumar, R. l.; Meiser, J. H.; Bloom, I. Glass-ceramic sealants for solid oxide fuel cells: Part I. Physical properties. *J. Mater. Res.* **1996,** 11, (6), 1489.

103. Iwahara, H.; Yajima, T.; Hibino, T.; Ozaki, K.; Suzuki, H. Protonic conduction in calcium, strontium, and barium zirconates. *Solid State Ionics* **1993,** 61, 65.

104. Hamakawa, S.; Hibino, T.; Iwahara, H. Electrochemical methane coupling using protonic conductors. *J. Electrochem. Soc.* **1993,** 140, (2), 459.

105. Norby, T.; Larring, Y. Mixed hydrogen ion-electronic conductors for hydrogen permeable membranes. *Solid State Ionics* **2000,** 136-137, 139.

106. Tan, X.; Liu, S.; Li, K.; Hughes, R. Theoretical analysis of ion permeation through mixed conducting membranes and its application to dehydrogenation reactions. *Solid State Ionics* **2000,** 138, 149.

107. Li, L.; Iglesia, E. Modeling and analysis of hydrogen permeation in mixed proton-electronic conductors. *Chem. Eng. Sci.* **2003,** 58, (10), 1977.

108. Song, S. J.; Wachsman, E. D.; Rhodes, J.; Dorris, S. E.; Balachandran, U. Numerical modeling of hydrogen permeation in chemical potential gradients. *Solid State Ionics* **2003,** 164, (1-2), 107.

109. Kharton, V. V.; Kovalesky, A. V.; Yaremchenko, A. A.; Figueiredo, F. M.; Naumovich, E. N.; Shaulo, A. L.; Marques, F. M. B. Surface modification of $La_{0.3}Sr_{0.7}CoO_{3-\delta}$ ceramic membranes. *J. Membr. Sci.* **2002,** 195, 277.

110. Poulsen, F. W. Method for calculating ionic and electronic defect concentrations in proton containing perovskites. *J. Solid State Chem.* **1999,** 143, 115.

111. Shima, D.; Haile, S. M. The influence of cation non-stoichiometry on the properties of undoped and gadolinia-doped barium cerate. *Solid State Ionic* **1997,** 97, 443.

112. Ma, G.; Shimura, T.; Iwahara, H. Ionic conduction and nonstoichiometry in $Ba_xCe_{0.90}Y_{0.10}O_{3-\alpha}$. *Solid State Ionics* **1998,** 110, 103.

113. Sharova, N. V.; Gorelov, V. P. Effect of cation nonstoichiometry on the properties of solid electrolyte BaxCe0.97Nd0.03O3-delta (0.90 <= x <= 1.10). *Russ. J. Electrochem.* **2004,** 40, (6), 639.

114. Dean, J. A., *Lange's Handbook of Chemistry*. Thirteenth ed.; McGraw-Hill: New York, 1985; p 1792.

BIOGRAPHICAL SKETCH

James Michael Rhodes was born to James F. and Paula A. Rhodes in Warren, Michigan, on February 18th, 1972. After enjoying growing up through elementary school in Michigan with his family (which included his sisters, Anne and Lynne), Jamie became a South Carolinian in the summer of 1983. He graduated from Greer High School in Greer, SC in 1990 as the salutatorian.

He chose to attend Clemson University in Clemson, SC starting in the fall of 1990. He earned a bachelor's degree in ceramic engineering from Clemson in May of 1994, graduating magna cum laude. He also graduated from the Calhoun Honors College at Clemson. After many wonderful years in the foothills of upstate South Carolina, he ventured south to the University of Florida.

His days in the sunshine state gave him the opportunity to meet and to marry the former Kristina Rose Abrahams on April 28th, 2001. After a few years of wedded bliss, Kristi and Jamie welcomed James Oliver Rhodes into the world on October 9th, 2004. Oliver will be a lasting reminder of his Gainesville experience.

I certify that I have read this study and that in my opinion it conforms to acceptable standards of scholarly presentation and is fully adequate, in scope and quality, as a dissertation for the degree of Doctor of Philosophy.

Eric D. Wachsman, Chairman
Professor of Materials Science and
Engineering

I certify that I have read this study and that in my opinion it conforms to acceptable standards of scholarly presentation and is fully adequate, in scope and quality, as a dissertation for the degree of Doctor of Philosophy.

Timothy J. Anderson
Professor of Chemical Engineering

I certify that I have read this study and that in my opinion it conforms to acceptable standards of scholarly presentation and is fully adequate, in scope and quality, as a dissertation for the degree of Doctor of Philosophy.

Anthony B. Brennan
Professor of Materials Science and
Engineering

I certify that I have read this study and that in my opinion it conforms to acceptable standards of scholarly presentation and is fully adequate, in scope and quality, as a dissertation for the degree of Doctor of Philosophy.

Paul H. Holloway
Professor of Materials Science and
Engineering

I certify that I have read this study and that in my opinion it conforms to acceptable standards of scholarly presentation and is fully adequate, in scope and quality, as a dissertation for the degree of Doctor of Philosophy.

Wolfgang M. Sigmund
Associate Professor of Materials Science
and Engineering

This dissertation was submitted to the Graduate Faculty of the College of Engineering and to the Graduate School and was accepted as partial fulfillment of the requirements for the degree of Doctor of Philosophy.

May 2005

Pramod Khargonekar

Pramod P. Khargonekar
Dean, College of Engineering

Winfred M. Phillips
Dean, Graduate School